Multipole-fluctuation pairing mechanism of $d_{x^2\text{-}y^2} + ig$ superconductivity in Sr_2RuO_4

Yutao Sheng,[1,2] Yu Li,[3] and Yi-feng Yang[1,2,4,*]

[1]*Beijing National Laboratory for Condensed Matter Physics and Institute of Physics, Chinese Academy of Sciences, Beijing 100190, China*
[2]*School of Physical Sciences, University of Chinese Academy of Sciences, Beijing 100049, China*
[3]*Kavli Institute for Theoretical Sciences, University of Chinese Academy of Sciences, Beijing 100190, China*
[4]*Songshan Lake Materials Laboratory, Dongguan, Guangdong 523808, China*

(Received 18 December 2021; revised 2 July 2022; accepted 16 August 2022; published 23 August 2022)

Despite many experimental and theoretical efforts, the pairing symmetry of superconductivity in Sr_2RuO_4 remains undecided. The accidentally degenerate $d_{x^2-y^2} + ig$ is consistent with most current experiments and seems to be one of the most probable candidates, but we still lack a satisfactory theoretical mechanism for its appearance. Here we construct a phenomenological model combining realistic electronic band structures and all symmetry-allowed multipole fluctuations as potential pairing glues and make a systematic survey of major pairing states within the Eliashberg framework. Our calculations show that $d_{x^2-y^2} + ig$ can arise naturally from the interplay of antiferromagnetic, ferromagnetic, and electric multipole fluctuations whose coexistence is manifested in previous experiments and calculations. Our work provides a physically reasonable basis supporting the possibility of $d_{x^2-y^2} + ig$ pairing in superconducting Sr_2RuO_4.

DOI: 10.1103/PhysRevB.106.054516

I. INTRODUCTION

For over two decades, superconductivity in Sr_2RuO_4 had been proposed to be of odd-parity spin-triplet pairing both in theory and in experiment [1–5]. This belief was recently overturned when refined nuclear magnetic resonance (NMR) [6–8] and polarized neutron scattering (PNS) [9] experiments detected a drop in the spin susceptibility below T_c. Muon spin relaxation (μSR) and polar Kerr effect revealed time-reversal symmetry breaking (TRSB) of the superconducting order parameter [10,11]. A line-node gap was then supported by specific heat [12–14], penetration depth [15], thermal conductivity [16,17], spin-lattice relaxation rate [18], and quasiparticle interference imaging from scanning tunneling microscope (STM) [19]. Candidate proposals of two-component TRSB order parameters include $d_{x^2-y^2} + ig$ [20,21], $s + id_{x^2-y^2}$ [22,23], $s + id_{xy}$ [24,25], chiral or helical or mixed p waves [4,26–35], $d_{xz} + id_{yz}$ [36], and exotic interorbital pairings [37–42].

Further constraints can be extracted from several of the latest experiments. A detailed NMR analysis reported an upper limit of the condensate magnetic response and excluded all purely odd-parity states (such as $p_x + ip_y$) [8]. STM measurements pointed toward a nodal direction along the zone diagonal, supporting a dominant $d_{x^2\text{-}y^2}$ component [19]. Although later analysis suggested that $s + id_{xy}$ with accidental nodes near the zone diagonal might also explain the STM data [25], it was often considered to be incompatible with the electronic structure of Sr_2RuO_4 [43]. In ultrasound experiments, a thermodynamic discontinuity was reported in the shear elastic modulus c_{66} [43,44], which excluded $s + id_{x^2-y^2}$. μSR measurements reported the split (unsplit) of the superconducting transition under uniaxial (hydrostatic) pressure [45,46] and supported the symmetry-protected $d_{xz} + id_{yz}$ pairing, but specific heat measurement fails to see the split under uniaxial pressure [47]. Moreover, $d_{xz} + id_{yz}$ normally requires a jump in the $(c_{11} - c_{22})/2$ modulus which was not observed in the ultrasound experiment.

Thus, the accidentally degenerate $d_{x^2-y^2} + ig$ seems to be the most probable one among all candidates [20]. It agrees with most of the above experiments, although a modification based on strain inhomogeneity might be needed to explain the absence of an evident-specific heat jump at the TRSB transition under uniaxial pressure [48,49]. However, the occurrence of $d_{x^2-y^2} + ig$ lacks a strong theoretical support so far. In particular, it is unclear how the g wave can arise and become accidentally degenerate with the dominant $d_{x^2\text{-}y^2}$ component. A recent theory can indeed derive the g wave but requires a sizable momentum-dependent spin-orbit coupling (SOC) beyond the first-principles prediction [21]. Hence, a fully consistent explanation of the pairing symmetry in Sr_2RuO_4 has not been achieved.

In this paper, we explore the possibility of $d_{x^2-y^2} + ig$ by constructing a general model Hamiltonian that combines realistic band structures from angle-resolved photoemission spectroscopy (ARPES) and multipole pairing interactions allowed by symmetry for the spin-orbit coupled Ru-4d electrons. The superconducting gap structures are then evaluated systematically by solving the linearized Eliashberg equations with antiferromagnetic (AFM), ferromagnetic (FM), electric multipole fluctuations and their mixtures. We find that the $d_{x^2-y^2} + ig$ (pseudospin) singlet pairing can actually be generated by the interplay of these three multipole pairing interactions within a reasonable parameter range. This provides a natural physical basis for the occurrence of $d_{x^2-y^2} + ig$. We

*yifeng@iphy.ac.cn

TABLE I. Multipole operators classified according to the irreducible representations Γ of D_{4h} point group based on the operator-equivalent technique. The $j = 5/2$ manifold contains operators from rank 0 to rank 5 (monopole $\mathbb{1}$, dipole J, quadrupole O, octupole T, hexadecapole H, dotriacontapole D), while multipole operators in $j = 3/2$ are up to rank 3 (monopole $\mathbb{1}$, dipole J, quadrupole O, octupole T). The subscript g marks inversion-symmetric representations and the superscripts $+/-$ denote time-reversal symmetric/antisymmetric ones. The subscripts of multipole operators are related to the tesseral harmonics in O_h group or cubic harmonics [54,56,57]. For simplicity, we have used the same symbols for both j spaces. More details are explained in Appendix A.

IR (Γ)	$\hat{Q}^{j=3/2,\Gamma\alpha}$	$\hat{Q}^{j=5/2,\Gamma\alpha}$
	Electric multipole operators	
A_{1g}^+	$\hat{\mathbb{1}}, \hat{O}_{20}$	$\hat{\mathbb{1}}, \hat{O}_{20}, \hat{H}_0, \hat{H}_4$
A_{2g}^+		$\hat{H}_{za}$
B_{1g}^+	$\hat{O}_{22}$	$\hat{O}_{22}, \hat{H}_2$
B_{2g}^+	$\hat{O}_{xy}$	$\hat{O}_{xy}, \hat{H}_{zb}$
E_g^+	$(\hat{O}_{xz}, \hat{O}_{yz})$	$(\hat{O}_{xz}, \hat{O}_{yz}), (\hat{H}_{xa}, \hat{H}_{ya}), (\hat{H}_{xb}, \hat{H}_{yb})$
	Magnetic multipole operators	
A_{1g}^-		$\hat{D}_4$
A_{2g}^-	$\hat{J}_z, \hat{T}_{za}$	$\hat{J}_z, \hat{T}_{za}, \hat{D}_{za1}, \hat{D}_{za2}$
B_{1g}^-	$\hat{T}_{xyz}$	$\hat{T}_{xyz}, \hat{D}_2$
B_{2g}^-	$\hat{T}_{zb}$	$\hat{T}_{zb}, \hat{D}_{zb}$
E_g^-	$(\hat{J}_x, \hat{J}_y), (\hat{T}_{xa}, \hat{T}_{ya}), (\hat{T}_{xb}, \hat{T}_{yb})$	$(\hat{J}_x, \hat{J}_y), (\hat{T}_{xa}, \hat{T}_{ya}), (\hat{T}_{xb}, \hat{T}_{yb}), (\hat{D}_{xa1}, \hat{D}_{ya1}), (\hat{D}_{xa2}, \hat{D}_{ya2}), (\hat{D}_{xb}, \hat{D}_{yb})$

will also briefly discuss the conditions for other pairing states within our theoretical framework.

II. MODEL

Crystal-field splitting and SOC are considered of equal importance in Sr_2RuO_4 [5,50,51]. To capture the pairing symmetry, it is convenient to construct a general model Hamiltonian based on the multipole representation of the pairing interactions. By the Stevens operator-equivalent technique, the multipole operators $\hat{Q}^{jkq}$ ($k = 0, 1, \ldots, 2j$; $q = -k, -k+1, \ldots, k$) for a given angular momentum j can be obtained from the $(2j+1) \times (2j+1)$ tensor operator $\hat{J}_{kq}$ satisfying [52,53]

$$\hat{J}_{kk} = (-1)^k \sqrt{\frac{(2k-1)!!}{(2k)!!}} (\hat{J}_+)^k,$$
$$[\hat{J}_\pm, \hat{J}_{kq}] = \sqrt{(k \mp q)(k \pm q + 1)} \hat{J}_{k,q\pm1} \; (q < k), \tag{1}$$

where $\hat{J}_\pm$ is the raising/lowering operator within the corresponding j subspace. These multipole operators are further projected into the irreducible representation (IR) Γ of the D_{4h} point group of Sr_2RuO_4 and denoted as $\hat{Q}^{j\Gamma\alpha}$ for the αth component in Γ [54,55]. Table I gives all multipole operators for the $j = 3/2$ and $5/2$ manifolds of Ru-4d electrons according to their IRs and ranks. The electric multipoles are of even rank and time-reversal symmetric and listed on the top of the table, while on the bottom are the magnetic multipoles (odd rank and time-reversal antisymmetric) [55,56]. More details

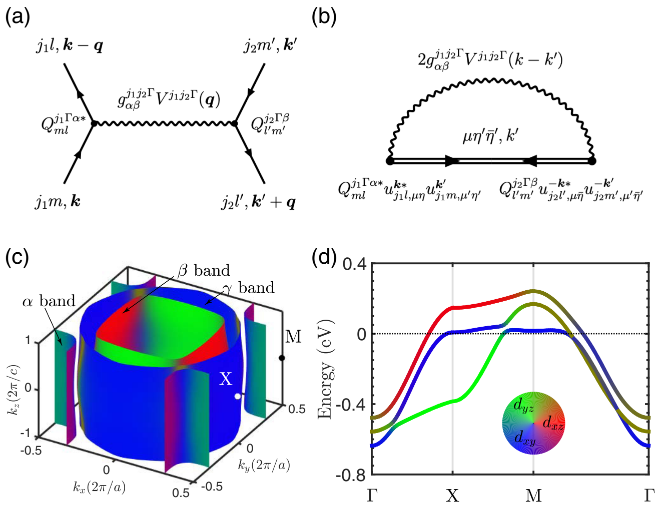

FIG. 1. (a) Illustration of the multipole interaction $\hat{Q}^{j_1\Gamma\alpha}\hat{Q}^{j_2\Gamma\beta}$. (b) The Feynman diagram of the anomalous self-energy $\psi_{\mu\eta\bar{\eta}}$ from multipole pairing interactions within the Eliashberg framework. We use $k = (\mathbf{k}, i\omega_n)$ for simplicity. (c) The 3D Fermi surfaces with (d_{xz}, d_{yz}, d_{xy}) orbital characters derived from the TB Hamiltonian H_{3D}. (d) Orbital-resolved band structures along a high-symmetry line on the $k_z = 0$ plane of the Brillouin zone. The inset shows the colors for three orbitals.

on the definition of these multipole operators can be found in Appendix A.

We then write a general interaction containing all symmetry-allowed multipole fluctuations as potential superconducting pairing glues:

$$\begin{aligned} H_{\text{int}} &= -\sum_{j_1 j_2}\sum_{\Gamma\alpha\beta}\sum_{\mathbf{q}} g_{\alpha\beta}^{j_1 j_2\Gamma} V^{j_1 j_2 \Gamma}(\mathbf{q}) \hat{Q}^{j_1\Gamma\alpha\dagger}(\mathbf{q}) \hat{Q}^{j_2\Gamma\beta}(\mathbf{q}) \\ &= -\sum_{j_1 j_2}\sum_{\Gamma\alpha\beta}\sum_{\mathbf{q},\mathbf{k},\mathbf{k}'}\sum_{lml'm'} g_{\alpha\beta}^{j_1 j_2\Gamma} V^{j_1 j_2 \Gamma}(\mathbf{q}) Q_{ml}^{j_1\Gamma\alpha *} Q_{l'm'}^{j_2\Gamma\beta} \\ &\quad \times c^\dagger_{j_1 l, \mathbf{k}-\mathbf{q}} c_{j_1 m,\mathbf{k}} c^\dagger_{j_2 l', \mathbf{k}'+\mathbf{q}} c_{j_2 m',\mathbf{k}'}, \end{aligned} \tag{2}$$

where $\hat{Q}^{j\Gamma\alpha}(\mathbf{q}) = \sum_{\mathbf{k},lm} Q_{lm}^{j\Gamma\alpha} c^\dagger_{jl,\mathbf{k}+\mathbf{q}} c_{jm,\mathbf{k}}$ and $c_{jm,\mathbf{k}}$ ($c^\dagger_{jm,\mathbf{k}}$) is the electron annihilation (creation) operator with $\mathbf{k}$ being the momentum and m the z projection of the total angular momentum j. The matrix elements $Q_{lm}^{j\Gamma\alpha}$ are normalized with $Q_{lm}^{j\Gamma\alpha} \to Q_{lm}^{j\Gamma\alpha}/\sqrt{\sum_{l'm'} |Q_{l'm'}^{j\Gamma\alpha}|^2}$ for comparison of different multipole fluctuations, $V^{j_1 j_2\Gamma}(\mathbf{q})$ is the momentum-dependent interaction vertex and $g_{\alpha\beta}^{j_1 j_2 \Gamma}$ controls the fluctuation strength between the multipole components $j_1\Gamma\alpha$ and $j_2\Gamma\beta$, as illustrated in Fig. 1(a). The values of $g_{\alpha\beta}^{j_1 j_2\Gamma}$ are highly restricted, as the multipole product should be projected to the identity representation of the crystallographic point group to keep the overall symmetry of the Hamiltonian. Thus, only multipoles belonging to the same IR (Γ) can be coupled, but they could have different angular momenta ($j_1 \neq j_2$) due to comparable SOC and crystal field potential [58,59]. For the two-dimensional IR $E_g^\pm$, such projection yields $(\hat{Q}_x^{j_1\Gamma\alpha}\hat{Q}_x^{j_2\Gamma\beta} + \hat{Q}_y^{j_1\Gamma\alpha}\hat{Q}_y^{j_2\Gamma\beta})/2$, which will be denoted as $\hat{Q}_r^{j_1\Gamma\alpha}\hat{Q}_r^{j_2\Gamma\beta}$ for simplicity. There are a total of six

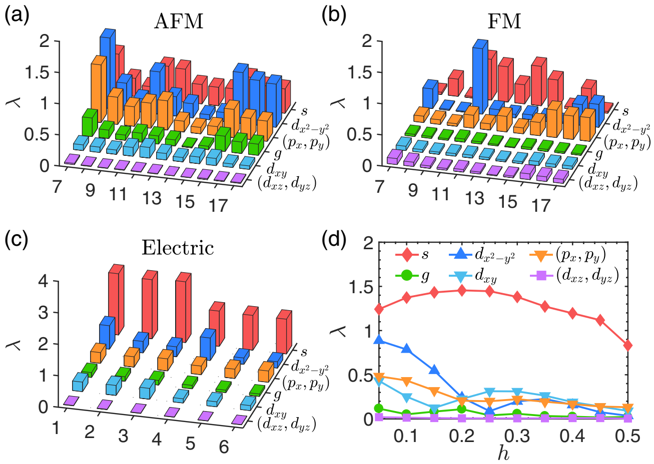

1	2	3	4	5	6	7	8	9
$\hat{\mathbb{1}}\hat{\mathbb{1}}$	$\hat{\mathbb{1}}\hat{O}_{20}$	$\hat{O}_{20}\hat{O}_{20}$	$\hat{O}_{22}\hat{O}_{22}$	$\hat{O}_{xy}\hat{O}_{xy}$	$\hat{O}_{rz}\hat{O}_{rz}$	$\hat{J}_z\hat{J}_z$	$\hat{J}_z\hat{T}_{za}$	$\hat{T}_{za}\hat{T}_{za}$
10	11	12	13	14	15	16	17	
$\hat{T}_{xyz}\hat{T}_{xyz}$	$\hat{T}_{zb}\hat{T}_{zb}$	$\hat{J}_r\hat{J}_r$	$\hat{J}_r\hat{T}_{ra}$	$\hat{J}_r\hat{T}_{rb}$	$\hat{T}_{ra}\hat{T}_{ra}$	$\hat{T}_{ra}\hat{T}_{rb}$	$\hat{T}_{rb}\hat{T}_{rb}$	

FIG. 2. Eigenvalues of six major pairing states, s (A_{1g}), $d_{x^2\text{-}y^2}$ (B_{1g}), (p_x, p_y) (E_u), g (A_{2g}), d_{xy} (B_{2g}), and (d_{xz}, d_{yz}) (E_g), for individual pairing interactions in $j = 3/2$ from (a) 11 AFM multipole channels with $\xi_{xy}^{\mathrm{AFM}} = 9.7$ Å, $\omega_{\mathbf{q}} = \omega_0^{\mathrm{AFM}} = 11.1$ meV, and $\mathbf{Q}_{\mathrm{AFM}} = (0.3, 0.3, 0)$; (b) 11 FM multipole channels with $\xi_{xy}^{\mathrm{FM}} = 2.5$ Å, $\omega_{\mathbf{q}} = v_0|\mathbf{q}|$, and $\mathbf{Q}_{\mathrm{FM}} = (0, 0, 0)$; (c) six electric multipole fluctuation channels with $\xi_{xy}^{\mathrm{E}} = \xi_{xy}^{\mathrm{AFM}}$, $\omega_{\mathbf{q}} = \omega_0^{\mathrm{E}} = \omega_0^{\mathrm{AFM}}$, and $\mathbf{Q}_{\mathrm{E}} = (0.2, 0.2, 0)$. (d) Eigenvalues of six major pairing states for averaged electric multipole fluctuations as a function of $\mathbf{Q}_{\mathrm{E}}$ along $(h, h, 0)$ direction. The s-wave state always dominates and has a maximal eigenvalue around $\mathbf{Q}_{\mathrm{E}} = (0.2, 0.2, 0)$. The table on the bottom lists all multipole fluctuation components for $j = 3/2$, sorted according to their IRs and ranks. The longitudinal correlation length is set to $\xi_z = 0.1\xi_{xy}$.

electric multipole fluctuation channels and 11 magnetic multipole fluctuation channels in the $j = 3/2$ manifold (listed at the bottom of Fig. 2), 23 electric components, and 38 magnetic components in the $j = 5/2$ manifold (bottom of Fig. 7); 15 electric and 30 magnetic j-mixed ($j_1 \neq j_2$) multipole channels (bottom of Fig. 8) that are allowed by symmetry in Sr_2RuO_4. For example, using the electric multipole operators listed in Table I, we can generate six electric multipole fluctuation channels for $j = 3/2$: $\hat{\mathbb{1}}\hat{\mathbb{1}}$, $\hat{\mathbb{1}}\hat{O}_{20}$, $\hat{O}_{20}\hat{O}_{20}$, $\hat{O}_{22}\hat{O}_{22}$, $\hat{O}_{xy}\hat{O}_{xy}$, and $\hat{O}_{rz}\hat{O}_{rz}$, which are listed at the bottom of Fig. 2 according to the IRs and ranks of the corresponding multipole operators.

The above procedures lay out a general phenomenological framework for studying electron pairing induced by multipole fluctuations. To apply it to Sr_2RuO_4, we consider the following three dimensional (3D) tight-binding (TB) model, $H_{3D} = H_{2D} + H_z$, where $H_{2D} = \sum_{\mathbf{k},s} \psi_s^\dagger(\mathbf{k}) h_0(\mathbf{k}, s)\psi_s(\mathbf{k})$ describes the k_z-independent band structure from ARPES measurements [60]. $\psi_s(\mathbf{k}) = [c_{xz,s}(\mathbf{k}), c_{yz,s}(\mathbf{k}), c_{xy,-s}(\mathbf{k})]^T$ is the basis of the low-lying Ru-4d t_{2g} orbitals (d_{xz}, d_{yz}, d_{xy}). We have

$$h_0(\mathbf{k}, s) = \begin{pmatrix} \epsilon_{\mathbf{k}}^{xz} - \mu_0 & \epsilon_{\mathbf{k}}^{\mathrm{off}} - is\lambda_{\mathrm{SOC}} & i\lambda_{\mathrm{SOC}} \\ \epsilon_{\mathbf{k}}^{\mathrm{off}} + is\lambda_{\mathrm{SOC}} & \epsilon_{\mathbf{k}}^{yz} - \mu_0 & -s\lambda_{\mathrm{SOC}} \\ -i\lambda_{\mathrm{SOC}} & -s\lambda_{\mathrm{SOC}} & \epsilon_{\mathbf{k}}^{xy} - \mu_0 \end{pmatrix}, \tag{3}$$

with $s = \pm$ for the spin and

$$\begin{aligned} \epsilon_{\mathbf{k}}^{xy} &= -2t_1\cos(k_x) - 2t_2\cos(k_y), \\ \epsilon_{\mathbf{k}}^{yz} &= -2t_2\cos(k_x) - 2t_1\cos(k_y), \\ \epsilon_{\mathbf{k}}^{xz} &= -2t_3(\cos(k_x) + \cos(k_y)) - 4t_4\cos(k_x)\cos(k_y) \\ &\quad - 2t_5(\cos(2k_x) + \cos(2k_y)), \\ \epsilon_{\mathbf{k}}^{\mathrm{off}} &= -4t_6\sin(k_x)\sin(k_y). \end{aligned} \tag{4}$$

The H_z term describes the hopping along the z direction and is introduced to deal with out-of-plane pairing such as (d_{xz}, d_{yz}). Under the same basis $\psi_s(\mathbf{k})$, it takes the form

$$H_z(\mathbf{k}) = -8t_0\cos(k_x/2)\cos(k_y/2)\cos(k_z/2). \tag{5}$$

The best ARPES fit yields $[t_1, t_2, t_3, t_4, t_5, t_6, \mu_0, \lambda_{\mathrm{SOC}}] = [0.145, 0.016, 0.081, 0.039, 0.05, 0, 0.122, 0.032]$ eV [60]. We choose $t_0 = 0.01$ eV so t_0/t_1 agrees with a previous study [61]. It should be noted that we have only considered $\mathbf{k}$-independent SOC, whose magnitude is consistent with density functional theory (DFT) calculations [21]. It has been shown previously that including different types of $\mathbf{k}$-dependent SOC may enhance certain particular pairing states, but to make them dominant requires the $\mathbf{k}$-dependent SOC to be at least one order higher in magnitude than those predicted by DFT [21,38]. Therefore, we will not discuss such possibility in this work. The resulting 3D Fermi surfaces of our model are plotted in Fig. 1(c), and the 2D orbital-resolved band structures are shown in Fig. 1(d) along a high symmetry line within the $k_z = 0$ plane of the Brillouin zone.

The above TB Hamiltonian also allows us to get a feeling about leading multipole fluctuations, which cannot be obtained currently from experiment [62–64]. As shown in Appendix B, calculations based on random phase approximation (RPA) for $j = 3/2$ yield two leading multipole correlations, $\langle\hat{J}_z\hat{J}_z\rangle$, $\langle\hat{T}_{ra}\hat{T}_{ra}\rangle$, in the AFM channel and four leading correlations, $\langle\hat{J}_z\hat{J}_z\rangle$, $\langle\hat{T}_{ra}\hat{T}_{ra}\rangle$, $\langle\hat{T}_{ra}\hat{T}_{rb}\rangle$, and $\langle\hat{T}_{rb}\hat{T}_{rb}\rangle$, in the FM channel. By contrast, electric multipole fluctuations are nearly unchanged for the Stoner factor $\alpha_S < 1$, implying that there is no electric instability. The definition of the Stoner factor is given in Appendix B. The leading multipoles are supposed to dominate the pairing interaction in the RPA approximation, but other components also should be present and have substantial contributions. Quite often, RPA cannot give a proper description of multipole fluctuations in real materials with strong electronic correlations. To have a systematic analysis of the electrons' pairing, we disentangle all multipole components allowed by symmetry and assume an empirical form of the interaction vertex [65,66],

$$V^{j_1 j_2 \Gamma}(\mathbf{q}, i\nu_n) = \frac{1}{1 + [\boldsymbol{\xi}\cdot(\mathbf{q} - \mathbf{Q})]^2 + |\nu_n|/\omega_{\mathbf{q}}}, \tag{6}$$

where ν_n is the bosonic Matsubara frequency, $\boldsymbol{\xi} = (\xi_{xy}, \xi_{xy}, \xi_z)$ is the anisotropic correlation length of corresponding multipole fluctuations, $\omega_{\mathbf{q}}$ is the fluctuation energy, and $\mathbf{Q}$ is the characteristic wave vector for AFM, FM, or electric fluctuations. These parameters may in principle vary with j_1, j_2, and Γ. Here we drop the labels for simplicity.

The above empirical form has the advantage of directly incorporating some important information of the AFM, FM, or electric fluctuations from experiments. It reflects the dynamical fluctuations of pairing interactions beyond mean-field approximation, which is often important in strongly correlated superconductors. Its exact form was initially proposed for the spin-fluctuation spectrum in cuprates and may be derived from a straightforward expansion of the momentum-dependent spin interaction [65–67]. It was later applied to other unconventional superconductors and has explained many of their important properties [68–74]. Here we further extend it to multipole fluctuations in Sr_2RuO_4 in the presence of SOC. This inevitably introduces many free parameters, so we will study each multipole fluctuation individually before proposing a form of their mixture to simplify the discussion on potential pairing states in reality.

III. ELIASHBERG EQUATIONS

Candidate pairing symmetries of the superconductivity can be analyzed using the linearized Eliashberg equations [67,71]:

$$
\begin{aligned}
Z_\mu(\mathbf{k}, i\omega_n) &= 1 + \frac{\pi T}{\omega_n}\sum_{\mu',n'}\oint_{\mathrm{FS}_{\mu'}}\frac{d\mathbf{k}'}{(2\pi)^3 v_{\mathbf{k}'_\mathrm{F}}}\mathrm{sgn}(\omega_{n'})K^{\mathrm{N}}_{\mu\mu'}(\mathbf{k}, i\omega_n; \mathbf{k}', i\omega_{n'}),\\
\lambda\psi_\mu(\mathbf{k}, i\omega_n) &= \pi T\sum_{\mu',n'}\oint_{\mathrm{FS}_{\mu'}}\frac{d\mathbf{k}'}{(2\pi)^3 v_{\mathbf{k}'_\mathrm{F}}}\psi_{\mu'}(\mathbf{k}', i\omega_{n'})\frac{K^{\mathrm{A}}_{\mu\mu'}(\mathbf{k}, i\omega_n; \mathbf{k}', i\omega_{n'})}{|\omega_{n'}Z_{\mu'}(\mathbf{k}', i\omega_{n'})|},
\end{aligned} \tag{7}
$$

where ω_n and $\omega_{n'}$ denote the fermionic Matsubara frequencies, μ and μ' are band indices, the integral with $\mathrm{FS}_{\mu'}$ is over the Fermi surface of band μ' with corresponding Fermi velocity $v_{\mathbf{k}'_\mathrm{F}}$, Z_μ is the renormalization function, and $\psi_\mu = \Delta_\mu Z_\mu$ is the anomalous self-energy related to the gap function Δ_μ. All bands are doubly degenerate with pseudospin $\eta = \pm$ and we only consider intraband pairing (singlet or triplet over pseudospin). Figure 1(b) shows the Feynman diagram for the anomalous self-energy ψ_μ. During our calculations, the kernel functions $K^{\mathrm{N}}_{\mu\mu'}$ and $K^{\mathrm{A}}_{\mu\mu'}$ can be determined from the interacting Hamiltonian H_{int} using the above empirical pairing interactions and take the following forms:

$$
\begin{aligned}
K^{\mathrm{N}}_{\mu\mu'}(\mathbf{k}, i\omega_n; \mathbf{k}', i\omega_{n'}) &= \sum_{\substack{j_1 j_2\Gamma\\ \alpha\beta}}\sum_{\substack{lml'm'\\ \eta\eta'}} g^{j_1j_2\Gamma}_{\alpha\beta}V^{j_1j_2\Gamma}(\mathbf{k}-\mathbf{k}', i\omega_n - i\omega_{n'})\mathrm{Re}\big[Q^{j_1\Gamma\alpha*}_{ml}Q^{j_2\Gamma\beta}_{l'm'}u^{\mathbf{k}*}_{j_1l,\mu\eta}u^{\mathbf{k}'}_{j_1m,\mu'\eta'}u^{\mathbf{k}'*}_{j_2l',\mu'\eta'}u^{\mathbf{k}}_{j_2m',\mu\eta}\big],\\
K^{\mathrm{A}}_{\mu\mu'}(\mathbf{k}, i\omega_n; \mathbf{k}', i\omega_{n'}) &= \sum_{\substack{j_1 j_2\Gamma\\ \alpha\beta}}\sum_{\substack{lml'm'\\ \eta}} g^{j_1j_2\Gamma}_{\alpha\beta}Q^{j_1\Gamma\alpha*}_{ml}Q^{j_2\Gamma\beta}_{l'm'}\big[V^{j_1j_2\Gamma}(\mathbf{k}-\mathbf{k}', i\omega_n - i\omega_{n'})u^{\mathbf{k}*}_{j_1l,\mu\eta}u^{\mathbf{k}'}_{j_1m,\mu'\eta}u^{-\mathbf{k}*}_{j_2l',\mu\bar{\eta}}u^{-\mathbf{k}'}_{j_2m',\mu'\bar{\eta}}\\
&\quad + V^{j_1j_2\Gamma}(\mathbf{k}+\mathbf{k}', i\omega_n + i\omega_{n'})u^{\mathbf{k}*}_{j_1l,\mu\eta}u^{-\mathbf{k}'}_{j_1m,\mu'\bar{\eta}}u^{-\mathbf{k}*}_{j_2l',\mu\bar{\eta}}u^{\mathbf{k}'}_{j_2m',\mu'\eta}\big],
\end{aligned} \tag{8}
$$

where $\hat{u}^{\mathbf{k}}$ is the matrix diagonalizing the 3D or 2D TB Hamiltonian, projected in the j representation. The linearized Eliashberg equations can be solved numerically by approximating $\Delta_\mu(\mathbf{k}) \equiv \Delta_\mu(\mathbf{k}, i\omega_n) \approx \Delta_\mu(\mathbf{k}, i\pi T_c)$ and using 1024 Matsubara frequencies, $41 \times 41 \times 41$ $\mathbf{k}$ meshes in the 3D Brillouin zone or 201×201 $\mathbf{k}$ meshes in the 2D Brillouin zone. Each eigenvector λ of Eqs. (7) corresponds to a single solution of electron pairing and gives the corresponding gap structure on the Fermi surfaces. The largest eigenvalue λ of ψ_μ at T_c determines the leading pairing state.

IV. INDIVIDUAL PAIRING INTERACTIONS

The results of individual multipole fluctuation channels are presented in Fig. 2 for $j = 3/2$ and Figs. 7 and 8 in Appendix D for $j = 5/2$ and j-mixed subspaces, respectively. We compare the eigenvalues of six major pairing states, s, $d_{x^2\text{-}y^2}$, (p_x, p_y), g, d_{xy}, (d_{xz}, d_{yz}), for the 3D Hamiltonian $H_{3\mathrm{D}}$ of Sr_2RuO_4. The parameter $g^{j_1j_2\Gamma}_{\alpha\beta}$ is chosen such that all multipole fluctuations are treated equally for each set of calculations.

For AFM fluctuations, inelastic neutron scattering experiments estimate $\xi^{\mathrm{AFM}}_{xy} = 9.7$ Å and $\omega_{\mathbf{q}} = \omega^{\mathrm{AFM}}_0 = 11.1$ meV at the AFM wave vector $\mathbf{Q}_{\mathrm{AFM}} = (0.3, 0.3, q_l)$ [62–64], where q_l will be set to zero in our calculations but its value shows no qualitative influence on our results. The longitudinal correlation length is set to $\xi^{\mathrm{AFM}}_z = 0.1\xi^{\mathrm{AFM}}_{xy}$ to reflect the absence of z-axis signal [63]. As shown in Fig. 2(a), among all 11 AFM multipole fluctuation channels for $j = 3/2$, $d_{x^2\text{-}y^2}$ or s are most supported. Two leading fluctuation channels from RPA analysis, $\hat{J}_z\hat{J}_z$ and $\hat{T}_{ra}\hat{T}_{ra}$, give predominant $d_{x^2\text{-}y^2}$-wave pairing. The subordinate channels, $\hat{J}_z\hat{T}_{za}$, $\hat{T}_{xyz}\hat{T}_{xyz}$, $\hat{T}_{ra}\hat{T}_{rb}$, $\hat{T}_{rb}\hat{T}_{rb}$, also support $d_{x^2\text{-}y^2}$, while the subordinate $\hat{T}_{zb}\hat{T}_{zb}$, $\hat{J}_r\hat{J}_r$, $\hat{J}_r\hat{T}_{ra}$, $\hat{J}_r\hat{T}_{rb}$ favor s wave and $\hat{T}_{za}\hat{T}_{za}$ favors (p_x, p_y) or $p_x + ip_y$. For $j = 5/2$ as shown in Fig. 7(a), the leading dipole component $\hat{J}_z\hat{J}_z$ supports $d_{x^2\text{-}y^2}$, while the leading dotriacontapole $\hat{D}_{za2}\hat{D}_{za2}$ supports s-wave pairing. Figure 8(a) gives the results for j-mixed AFM fluctuations. We see s and $d_{x^2\text{-}y^2}$ are also the two most favored pairing states.

FM pairing interactions have previously been considered because Sr_2RuO_4 has similar electronic structures as the itinerant ferromagnets $SrRuO_3$ and $Sr_4Ru_3O_{10}$ and the metamagnet $Sr_3Ru_2O_7$ [5,75]. A short-range FM order was reported in experiments in Co-doped Sr_2RuO_4, indicating that Sr_2RuO_4 might be near a FM instability [76]. PNS experiments in Sr_2RuO_4 also reported a broad FM response [64], giving $\mathbf{Q}_{\mathrm{FM}} = (0, 0, 0)$, $\xi^{\mathrm{FM}}_{xy} = 2.5$ Å and a characteristic energy $\omega^{\mathrm{FM}}_0 = 15.5$ meV. Since there are no further experimental details for the FM multipole fluctuations, we will simply take $\omega_{\mathbf{q}} = v_0|\mathbf{q}|$ and choose v_0 such that $\omega_{\mathbf{q}}$ reaches the order of $\omega_0^{\rm FM}$ at the zone boundary. A slight variation of v_0 makes no qualitative change on our main conclusions. Figure 2(b) shows the typical results of six major pairing states induced by FM pairing interactions for $j = 3/2$. Similarly, we find predominant $d_{x^2\text{-}y^2}$-wave pairing from leading dipole fluctuations $\hat{J}_z\hat{J}_z$ and (p_x, p_y) waves from leading octupoles $\hat{T}_{ra}\hat{T}_{ra}$, $\hat{T}_{ra}\hat{T}_{rb}$, and $\hat{T}_{rb}\hat{T}_{rb}$, while the s wave is supported by some subordinate multipole channels. For $j = 5/2$ in Fig. 7(b), the leading dipole $\hat{J}_z\hat{J}_z$ favors the s waves, while the leading dotriacontapoles $\hat{D}_{ra1}\hat{D}_{ra1}$ and $\hat{D}_{rb}\hat{D}_{rb}$ support (p_x, p_y) waves. In Fig. 8(b), s and $d_{x^2\text{-}y^2}$ are supported by most j-mixed FM channels.

Electric fluctuations may arise from the multiorbital nature of Sr_2RuO_4 [77–81] and have a similar interaction vertex as AFM ones, but with $\mathbf{Q}_{\rm E} = (0.2, 0.2, 0)$, $\xi_{xy}^{\rm E} = \xi_{xy}^{\rm AFM}$, and $\omega_0^{\rm E} = \omega_0^{\rm AFM}$. As shown in Fig. 2(c), all six multipole channels for $j = 3/2$ support s-wave pairing, which is robust under the tuning of $\xi_{xy}^{\rm E}$ and $\omega_0^{\rm E}$. Figure 2(d) plots the eigenvalues of six major pairing states as a function of $\mathbf{Q}_{\rm E}$ along the (110) direction. We see that the s-wave pairing always has a much larger eigenvalue than others. This is expected since superconductivity induced by charge fluctuations is typically s wave. But, quite interestingly, the eigenvalue of s reaches a maximum around $\mathbf{Q}_{\rm E} = (0.2, 0.2, 0)$, exactly the wave vector proposed by the RPA charge susceptibility [81], implying a potential role of electric multipole fluctuations in superconducting Sr_2RuO_4. For $j = 5/2$ and j-mixed subspaces, Figs. 7(c) and 8(c) show that the s-wave pairing is always supported by leading electric multipole fluctuations.

All together, s and $d_{x^2\text{-}y^2}$ are most supported by individual multipole pairing interactions, while the remaining four are less favored. Thus, to discuss the possibility of g and the other three pairing states, it is necessary to go beyond individual multipole channels and consider some mixed form, which is reasonable given their coexistence. To proceed, we first note that all but (d_{xz}, d_{yz}) are m_z symmetric, i.e., symmetric about the $k_z = 0$ plane, whose relative importance can be evaluated in 2D. By contrast, the m_z-antisymmetric (d_{xz}, d_{yz}) or $d_{xz} + id_{yz}$ pairing state requires 3D calculations as performed above, but it is not favored because our TB Hamiltonian $H_{\rm 3D}$ is only weakly dispersive along k_z direction. We find this conclusion quite robust against reasonable tuning of t_0 and ξ_z within our framework. As an example, we give the results with an artificially enhanced $\xi_z = \xi_{xy}$ for $j = 3/2$ in Appendix C. In the literature, it has been proposed that $d_{xz} + id_{yz}$ may become dominant if a sizable $\mathbf{k}$-dependent SOC of E_g representation is included [38], which induces interorbital hopping along the z direction but has to be more than one order of magnitude higher than that of DFT prediction [21]. Hence, we will no longer consider $d_{xz} + id_{yz}$ in the following section to reduce computational efforts by performing calculations only in 2D.

V. MIXED PAIRING INTERACTIONS

From now on, we will focus on the 2D Hamiltonian $H_{\rm 2D}$. In real materials, different multipole fluctuations may coexist, so we must consider their possible combinations, namely, a mixed pairing interaction of AFM, FM, and electric multipole fluctuations such as

$$V_{\rm mix} = r_1 V^{\rm AFM} + r_2 V^{\rm FM} + r_3 V^{\rm E}, \tag{9}$$

where $V^{\rm AFM}$, $V^{\rm FM}$, and $V^{\rm E}$ denote the AFM, FM, and electric multipole pairing interactions, respectively, and r_i controls their relative strength. There may exist different combinations of individual multipole channels, but a natural one without much *a priori* knowledge is to average each term over all multipole components in their respective $j = 3/2$, $5/2$, or j-mixed subspaces. This work will focus on this particular form of the pairing interaction. But to examine the robustness of our results for other possible combinations, we also show in Appendix E the results for pairing interactions averaged only over $j = 3/2$ or over both $j = 3/2$ and $5/2$ subspaces. All other parameters are set to be the same as discussed in the previous section.

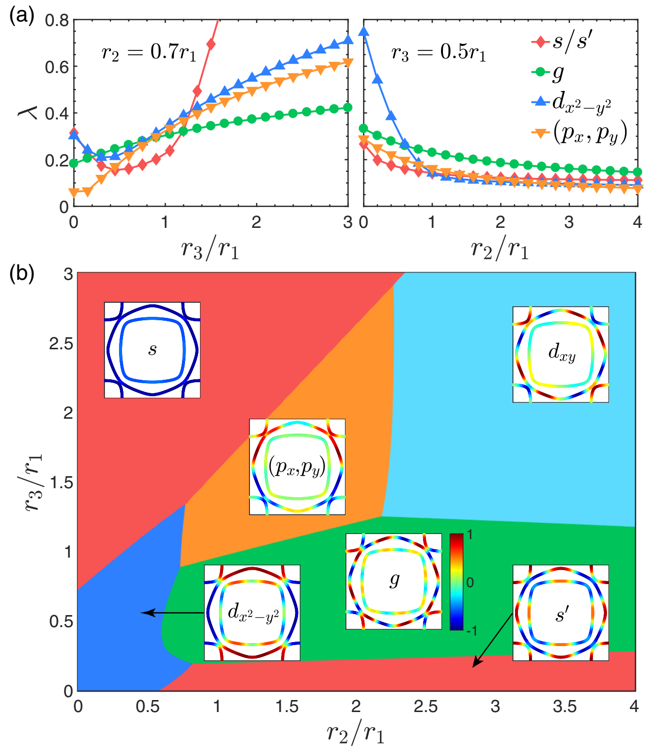

FIG. 3. (a) Eigenvalues of s/s', g, $d_{x^2\text{-}y^2}$, and (p_x, p_y) pairing states as a function of the ratio r_3/r_1 at $r_2/r_1 = 0.7$ and r_2/r_1 at $r_3/r_1 = 0.5$ for a mixed AFM, FM, and electric pairing interaction. (b) Theoretical phase diagram of predominant pairing states on the plane of r_2/r_1 and r_3/r_1. The insets show corresponding gap structures in each region.

The resulting phase diagram including $j = 3/2$, $5/2$, and j-mixed terms is plotted in Fig. 3, together with two examples of the largest eigenvalues of four major pairing states and their variations with the ratio r_2/r_1 or r_3/r_1. The $d_{x^2\text{-}y^2}$-wave is seen to extend from the origin ($r_2 = r_3 = 0$) to cover a major part of the phase diagram with dominant AFM multipole fluctuations ($r_2/r_1 < 0.6$, $r_3/r_1 < 0.7$). A nodal s wave is induced by a moderate FM pairing interaction ($r_2/r_1 > 0.6$), but for a stronger electric interaction ($r_3/r_1 > 0.7$) we find a predominant nodeless s wave. For distinction, we will use s' to denote a nodal s wave in the following. As discussed earlier, $d_{x^2\text{-}y^2}$ and s (or s') are major pairing states for dominant AFM, FM, or electric multipole fluctuations. In the absence of electric fluctuations ($r_3 = 0$), the resulting $d_{x^2\text{-}y^2}$ or s' waves agree well with previous work [22]. Quite surprisingly, g-wave pairing is seen in Fig. 3 to govern a large portion of the phase diagram where both FM and electric multipole fluctuations are of equal importance as the AFM ones.

Thus, within our framework, the accidentally degenerate $d_{x^2-y^2} + ig$ pairing may exist at the phase boundary with a somewhat weaker FM pairing interaction than the AFM one, namely, $r_2/r_1 \approx 0.6$. However, a moderate electric pairing interaction ($0.2 < r_3/r_1 < 0.8$) is also needed. If the electric fluctuations are too weak or too strong, a two-component $s' + id_{x^2-y^2}$ or $s + id_{x^2-y^2}$ might appear but is inconsistent with the ultrasound experiments [43,44]. The other two states, (p_x, p_y) and d_{xy}, require even stronger FM or electric fluctuations than AFM ones. In all cases, electric multipole fluctuations, such as zero-rank charge fluctuations, seem to play a crucial role in superconducting Sr_2RuO_4, and should be better examined by future x-ray diffraction or Raman experiments [82–86].

The emergence of a g wave is robust for such mixed AFM, FM, and electric pairing interactions. Appendix E shows the phase diagrams of two other examples of averaged pairing interactions. In the first case, we consider only the $j = 3/2$ subspace and take an averaged pairing interaction over all multipole fluctuations; in the second case, we take the average over both $j = 3/2$ and $5/2$ subspaces. The phase diagrams are shown in Fig. 9 and found qualitatively the same. The downshift of the phase boundaries in Fig. 3(b) indicates that the s-wave pairing is more promoted by the j-mixed multipole interaction. Nevertheless, the g-wave state still covers a large portion of the phase diagram with strong AFM fluctuations and moderate FM and electric ones, where $d_{x^2\text{-}y^2}$ and s (or s') solutions supported by individual multipole fluctuations are suppressed. We thus conclude that the competition and interplay of AFM, FM, and electric multipole fluctuations may provide a mechanism for the unusual $d_{x^2-y^2} + ig$ pairing in Sr_2RuO_4. Whether or not this reflects the true situation in real materials requires future experimental scrutiny.

To have an idea of the gap structures for these pairing states, Fig. 4 presents their projection (normalized) on the 2D Fermi surfaces and evolution with the azimuth ϕ. Both $d_{x^2\text{-}y^2}$ and g show clear symmetry-protected nodes on three bands along the zone diagonal ($\phi = \pm\pi/4$ and $\pm 3\pi/4$). The resulting $d_{x^2-y^2} + ig$ gap also has nodes along the zone diagonal, which is protected by symmetry and fits well to the STM data [19]. Quite unexpectedly, we also find that the s' wave can change signs or have gap minima near the zone diagonal. This interesting feature arises from the particular orbital character of the three bands. Along the diagonal direction, the α band contains a contribution only from $|j = \frac{3}{2}, j_z = \pm\frac{3}{2}\rangle$ and $|\frac{5}{2}, \pm\frac{5}{2}\rangle$, the β band contains only $|\frac{5}{2}, \pm\frac{3}{2}\rangle$ and $|\frac{5}{2}, \pm\frac{5}{2}\rangle$, and the γ band contains only $|\frac{3}{2}, \pm\frac{1}{2}\rangle$ and $|\frac{5}{2}, \pm\frac{1}{2}\rangle$. Hence, as an example, an s-wave pairing supported by multipole fluctuations of $j = 3/2$, $j_z = \pm 1/2$, or $j_z = \pm 3/2$ must have nodes along the zone diagonal on the β, α, or γ band, respectively. This may give rise to the gap minima after other contributions are included. Consequently, the two-component $s' + id_{x^2-y^2}$ can also exhibit gap minima near the zone diagonal. If we assume the two components have the same magnitude, we may obtain a gap structure in Fig. 4(d), where the relative gap ratio is $|\Delta_{\pi/4}/\Delta_{\max}| \approx 0.22, 0.45, 0.34$ for α, β, γ bands, respectively. Note that a previous STM experiment has an energy resolution of about 75 μeV, which is roughly 21% of the measured gap of 350 μeV [19]. Thus, it is impossible for the STM alone to exclude $s' + id_{x^2-y^2}$ if the s' component is only moderate compared to $d_{x^2\text{-}y^2}$ component. The ultrasound experiment is then crucial.

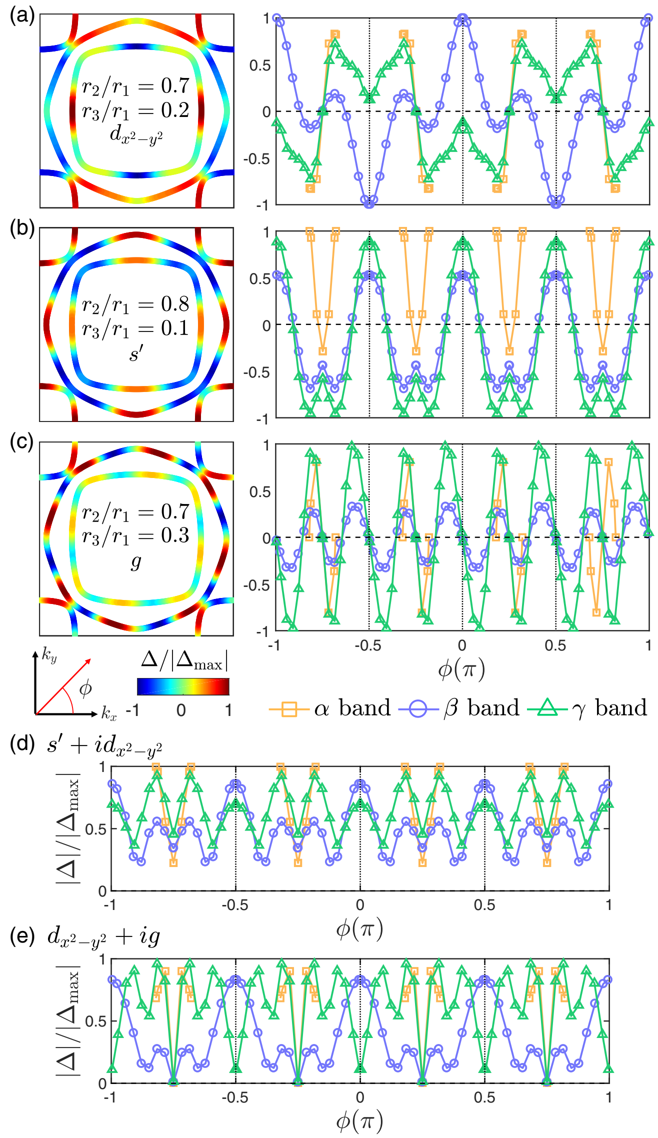

FIG. 4. Typical gap structures of (a) $d_{x^2\text{-}y^2}$, (b) s', and (c) g-wave pairing states and their evolutions with the azimuth ϕ. (d) Gap magnitude of a typical $s' + id_{x^2-y^2}$ pairing state constructed from (a), (b) as a function of the azimuth ϕ, showing local gap minima along the zone diagonal ($\phi = \pm\pi/4$ and $\pm 3\pi/4$) on all three bands. (e) Gap magnitude of a typical $d_{x^2-y^2} + ig$ pairing state from (b), (c) as a function of the azimuth ϕ, showing the symmetry-protected nodes along the zone diagonal.

VI. DISCUSSION AND CONCLUSIONS

Our results provide a potential physical basis for the possibility of $d_{x^2-y^2}+ig$ pairing in superconducting Sr_2RuO_4. But there are also proposals supporting other pairing states in the literature. For clarity, we give a brief summary in this section on current experimental and theoretical situations of several major candidates of two-component order parameters that break the time-reversal symmetry, including p_x+ip_y, $d_{xz}+id_{yz}$, $s'+id_{x^2-y^2}$, $s+id_{xy}$, and $d_{x^2-y^2}+ig$.

The purely odd-parity p_x+ip_y paring was recently excluded by a series of NMR [6–8] and PNS [9] experiments. A mixed-parity state has been proposed in the quasi-1D limit [31], which has accidental nodes along the zone diagonal consistent with the STM experiment [19]. However, the odd-parity component requires a jump in the shear elastic modulus $(c_{11}-c_{12})/2$, which was not observed in the ultrasound experiment, at least within the current accuracy [43,44]. In our theory, the p_x+ip_y paring is only supported by several FM fluctuation components such as the octupoles $\hat{T}_{ra}\hat{T}_{ra}$, $\hat{T}_{ra}\hat{T}_{rb}$, $\hat{T}_{rb}\hat{T}_{rb}$ of $j=3/2$, and therefore only appears for relatively strong FM and electric fluctuations in the unphysical regions of $r_2/r_1\approx 1-2$ and $r_3/r_1\approx 1-3$.

The $d_{xz}+id_{yz}$ pairing is typically unfavored due to the quasi-2D Fermi surface topology of Sr_2RuO_4, but may be stabilized if a sizable momentum-dependent E_g-SOC is included [38]. The latter could give rise to a spin-triplet odd-orbital $(d_{xz}+id_{yz})$-like pairing that can explain the Knight shift drop below T_c [87–89], but the required E_g-SOC is at least one order of magnitude higher than that predicted by DFT [21]. The $d_{xz}+id_{yz}$ gap is featured with horizontal line nodes on the $k_z=0$ plane [90], so it is supposed to cause spin resonance at $q_l=0$, which is, however, absent according to recent neutron scattering experiments [91,92]. It is also inconsistent with the ultrasound experiment showing no evident jump in $(c_{11}-c_{12})/2$ [43,44]. The $d_{xz}+id_{yz}$ pairing was mainly supported by μSR measurements that reported the splitting of superconductivity and TRSB under uniaxial pressure as opposed to hydrostatic pressure [45,46]. However, this splitting was questioned by specific heat measurements, which found no sign of bulk phase transition induced by uniaxial pressure [47]. More accurate experiments will be needed to clarify how exactly superconductivity evolves under pressure. In our calculations, the SOC is **k** independent and has a magnitude consistent with the DFT prediction. Thus, the $d_{xz}+id_{yz}$ pairing is always unfavored within our framework.

The $d_{x^2\text{-}y^2}$ wave has the desired vertical line nodes revealed by thermal conductivity [17] and nodes or gap minima on α and β bands in STM measurements [19]. From our calculations, it is indeed supported by AFM fluctuations and can form a two-component order parameter with accidentally degenerate s' or g in the presence of moderate FM and electric fluctuations. An $s'+id_{x^2-y^2}$ has been proposed in previous theory but was nodeless along the zone diagonal [22]. By contrast, our derived $s'+id_{x^2-y^2}$ can have nodes or gap minima near the 2D zone diagonal and may agree with STM. But $s'+id_{x^2-y^2}$ seems inconsistent with ultrasound experiment, where the observed thermodynamic jump of the shear elastic modulus $\delta c_{66}\propto\alpha_4^2$ reflects the coupling term $\alpha_4 u_{xy}(\Delta^*_{s'}\Delta_{d_{x^2-y^2}}+\Delta^*_{d_{x^2-y^2}}\Delta_{s'})$ between the strain u_{xy} and two superconducting components in the Landau free energy [43,44]. Such a coupling is prohibited by symmetry because $B_{2g}(u_{xy})\otimes A_{1g}(\Delta_{s'})\otimes B_{1g}(\Delta_{d_{x^2-y^2}})=A_{2g}\neq A_{1g}$.

To overcome this problem, an accidentally degenerate $s'+id_{xy}$ pairing has been proposed by taking into consideration the nearest-neighbor Coulomb repulsion [24], which is nodeless on the α band but has gap minima on the γ band along the azimuthal $\phi=0.15\pi$ direction. A recent analysis suggested that this $s'+id_{xy}$ gap structure could well fit the Bogoliubov quasiparticle interference pattern in STM measurements [25] and might be a competitive candidate for the pairing symmetry of superconducting Sr_2RuO_4. Calculations of the spin and charge susceptibilities indicated that the primary role of nearest-neighbor Coulomb repulsion is to enhance the electric fluctuations over the magnetic ones [24]. It thus corresponds to increase r_3/r_1 in our theory. In this sense, their result is consistent with our phase diagram, where d_{xy} can indeed become dominant at large $r_3/r_1>1$. But within our framework, it also requires very strong FM fluctuations ($r_2/r_1>2$), which is not realistic in experiments [64].

An interorbital spin-triplet $d_{x^2-y^2}+ig$ state has been proposed by including a sizable momentum-dependent B_{2g}-SOC about 20 times higher than that predicted by DFT [21]. It is different from our pseudospin singlet $d_{x^2-y^2}+ig$ solution which is a mixture of spin-singlet even-orbital and spin-triplet odd-orbital pairings but dominated by the spin-singlet component with a **k**-independent SOC of reasonable magnitude. In any case, $d_{x^2-y^2}+ig$ has the desired nodal structures for STM and the required symmetry $(B_{2g}(u_{xy})\otimes B_{1g}(\Delta_{d_{x^2-y^2}})\otimes A_{2g}(\Delta_g)=A_{1g})$ by ultrasound experiment, and may also find signatures in impurity scattering [93,94] or heat capacity [95]. However, as for all accidentally degenerate pairing states, $d_{x^2-y^2}+ig$ also suffers from the difficulty in explaining the observed unsplitting of the transition under hydrostatic pressure [45,46], as well as the lack of a large specific heat jump at the TRSB transition under uniaxial pressure [47]. It has been argued that the unsplit transition under hydrostatic pressure can be accounted for by proper assumption of the Landau-Ginzburg parameters [48] and a modified $d_{x^2-y^2}+ig$ scenario based on strain inhomogeneity near dislocations or domain walls may explain the lack of specific heat jump and the accidental degeneracy [48,49]. Unfortunately, these effects cannot be easily parameterized in our calculations, so a quantitative justification of their analyses is not immediately possible. On the other hand, on a very crude level, one may expect that hydrostatic pressure tends to modify all parameters in the Hamiltonian, which may increase the bandwidth but keep the ratios r_2/r_1 and r_3/r_1 less affected. If this is the case, one may expect that the system could be driven away from magnetic instabilities, so T_c decreases but the superconductivity stays near the boundary of $d_{x^2\text{-}y^2}$ and g waves with an unsplit transition. Under uniaxial strain, the system is driven toward an incommensurate spin-density-wave (SDW) instability as proposed in experiments [45], which may primarily enhance (for small strain) AFM fluctuations or r_1. As shown in Fig. 3(a), starting from the g-dominant region, the eigenvalue of $d_{x^2\text{-}y^2}$ increases more rapidly with decreasing r_2/r_1 and r_3/r_1, while that of the g wave varies only slightly. This would lead to an increase of T_c in the $d_{x^2\text{-}y^2}$ pairing channel before it reaches a maximum

TABLE II. Definition of multipole operators in Table I based on the operator-equivalent technique, which are classified according to the irreducible representations Γ of D_{4h} point group. The $j = 5/2$ manifold contains operators from rank 0 to rank 5 (monopole $\mathbb{1}$, dipole J, quadrupole O, octupole T, hexadecapole H, dotriacontapole D), while multipole operators in $j = 3/2$ are up to rank 3 (monopole $\mathbb{1}$, dipole J, quadrupole O, octupole T). For simplicity, we have used the same symbols for both j spaces. They have, in principle, different bases and representation matrices.

	IR(Γ)	α	$\hat{Q}^{j\Gamma\alpha}$	Basis
Electric	A_{1g}^+	1	$\hat{\mathbb{1}}$	$\hat{J}_{00}$
		2	$\hat{O}_{20}$	$\hat{J}_{20}$
		3	$\hat{H}_0$	$(\sqrt{7}\hat{J}_{40} + \sqrt{5}\hat{J}_{44c})/\sqrt{12}$
		4	$\hat{H}_4$	$(\sqrt{5}\hat{J}_{40} - \sqrt{7}\hat{J}_{44c})/\sqrt{12}$
	A_{2g}^+	1	$\hat{H}_{za}$	$\hat{J}_{44s}$
	B_{1g}^+	1	$\hat{O}_{22}$	$\hat{J}_{22c}$
		2	$\hat{H}_2$	$-\hat{J}_{42c}$
	B_{2g}^+	1	$\hat{O}_{xy}$	$\hat{J}_{22s}$
		2	$\hat{H}_{zb}$	$\hat{J}_{42s}$
	E_g^+	1	$\hat{O}_{xz}, \hat{O}_{yz}$	$\hat{J}_{21c}, \hat{J}_{21s}$
		2	$\hat{H}_{xa}, \hat{H}_{ya}$	$(-\hat{J}_{43c} + \sqrt{7}\hat{J}_{41c})/\sqrt{8}, (\hat{J}_{43s} + \sqrt{7}\hat{J}_{41s})/\sqrt{8}$
		3	$\hat{H}_{xb}, \hat{H}_{yb}$	$(-\sqrt{7}\hat{J}_{43c} - \hat{J}_{41c})/\sqrt{8}, (\sqrt{7}\hat{J}_{43s} - \hat{J}_{41s})/\sqrt{8}$
Magnetic	A_{1g}^-	1	$\hat{D}_4$	$\hat{J}_{54s}$
	A_{2g}^-	1	$\hat{J}_z$	$\hat{J}_{10}$
		2	T_{za}	$\hat{J}_{30}$
		3	D_{za1}	$\hat{J}_{50}$
		4	D_{za2}	$\hat{J}_{54c}$
	B_{1g}^-	1	$\hat{T}_{xyz}$	$\hat{J}_{32s}$
		2	D_2	$-\hat{J}_{52s}$
	B_{2g}^-	1	$\hat{T}_{zb}$	$\hat{J}_{32c}$
		2	$\hat{D}_{zb}$	$\hat{J}_{52c}$
	E_g^-	1	$\hat{J}_x, \hat{J}_y$	$\hat{J}_{11c}, \hat{J}_{11s}$
		2	$\hat{T}_{xa}, \hat{T}_{ya}$	$(\sqrt{5}\hat{J}_{33c} - \sqrt{3}\hat{J}_{31c})/\sqrt{8}, (-\sqrt{5}\hat{J}_{33s} - \sqrt{3}\hat{J}_{31s})/\sqrt{8}$
		3	$\hat{T}_{xb}, \hat{T}_{yb}$	$(\sqrt{3}\hat{J}_{33c} + \sqrt{5}\hat{J}_{31c})/\sqrt{8}, (-\sqrt{3}\hat{J}_{33s} + \sqrt{5}\hat{J}_{31s})/\sqrt{8}$
		4	$\hat{D}_{xa1}, \hat{D}_{ya1}$	$(3\sqrt{14}\hat{J}_{55c} - \sqrt{70}\hat{J}_{53c} + 2\sqrt{15}\hat{J}_{51c})/16, (3\sqrt{14}\hat{J}_{55s} + \sqrt{70}\hat{J}_{53s} + 2\sqrt{15}\hat{J}_{51s})/16$
		5	$\hat{D}_{xa2}, \hat{D}_{ya2}$	$(\sqrt{10}\hat{J}_{55c} + 9\sqrt{2}\hat{J}_{53c} + 2\sqrt{21}\hat{J}_{51c})/16, (\sqrt{10}\hat{J}_{55s} - 9\sqrt{2}\hat{J}_{53s} + 2\sqrt{21}\hat{J}_{51s})/16$
		6	$\hat{D}_{xb}, \hat{D}_{yb}$	$(\sqrt{30}\hat{J}_{55c} + \sqrt{6}\hat{J}_{53c} - 2\sqrt{7}\hat{J}_{51c})/8, (\sqrt{30}\hat{J}_{55s} - \sqrt{6}\hat{J}_{53s} - 2\sqrt{7}\hat{J}_{51s})/8$

near the SDW transition. At the same time, the g-wave component should remain less affected, which explains the splitting of the superconducting transition and the nearly unchanged T_{TRSB} induced by the g-wave channel below T_c. In this sense, our calculations are consistent with the pressure experiments, but more elaborated analyses with realistic parametrizations are needed for a final justification.

Putting together, $d_{x^2-y^2} + ig$ seems to be a most probable candidate for superconducting pairing in Sr_2RuO_4, at least within our framework. It may arise naturally from a mixed pairing interaction of AFM, FM, and electric multipole fluctuations of reasonable magnitudes. Our results provide a plausible explanation of the pairing symmetry in superconducting Sr_2RuO_4 and pose a challenge for future experiments to examine the role of different multipole fluctuations. Our theory may also be applied to other unconventional superconductors.

ACKNOWLEDGMENTS

This work was supported by the National Natural Science Foundation of China (NSFC Grants No. 11974397 and No. 12174429), the National Key Research and Development Program of MOST of China (Grant No. 2017YFA0303103), the Strategic Priority Research Program of the Chinese Academy of Sciences (Grant No. XDB33010100), the China Postdoctoral Science Foundation (Grant No. 2020M670422), and the Youth Innovation Promotion Association of CAS.

APPENDIX A: MULTIPOLE OPERATORS

Definitions of the multipole operators under the D_{4h} point group are listed in Table II and formed by the Hermitian tensor operators (for $q \neq 0$)

$$\hat{J}_{kqc} = \frac{1}{\sqrt{2}}[(-1)^q\hat{J}_{kq} + \hat{J}_{k,-q}],$$
$$\hat{J}_{kqs} = \frac{1}{\sqrt{2}i}[(-1)^q\hat{J}_{kq} - \hat{J}_{k,-q}]. \quad (A1)$$

For $q = 0$, $\hat{J}_{k0}$ is itself Hermitian. Different notations have been used for multipole operators in the literature [54–56,96,97]. Here we follow the convention in Ref. [56] and use the tesseral harmonics in the O_h point group or cubic harmonics as the basis [54,57]. For 1D or 2D IR of O_h, the subscript denotes the tesseral harmonics $Z_{kq}(\hat{\mathbf{r}})$. For 3D IR of O_h, the subscripts in $(\hat{O}_{xz}, \hat{O}_{yz}, \hat{O}_{xy})$ represent the basis function (zx, yz, xy), while other multipoles are marked by the subscript (x, y, z) with additional $a\,(b)$ denoting the

$T_{1g/u}$ ($T_{2g/u}$) IR, 1 (2) for different equal rank basis in the same IR, and g/u for inversion symmetric/antisymmetric. For instance, $(\hat{O}_{22}, \hat{O}_{20})$ in the E_g IR correspond to tesseral harmonics $r^2 Z_{22}(\hat{\mathbf{r}}) \propto x^2 - y^2$ and $r^2 Z_{20}(\hat{\mathbf{r}}) \propto 3z^2 - r^2$, respectively; $(\hat{D}_{xa1}, \hat{D}_{ya1}, \hat{D}_{za1})$ correspond to the first basis in T_{1u} IR [54,56,96,98]. For simplicity, we have dropped the label j of the total angular momentum. Multipole operators belonging to different j spaces may have the same notations but different representation matrices. As examples, the matrices for the dipole $\hat{J}_z$ and octupoles $\hat{T}_{xa}$, $\hat{T}_{xyz}$ are

$$\hat{J}_z = \frac{1}{2\sqrt{5}} \begin{pmatrix} -3 & & & \\ & -1 & & \\ & & 1 & \\ & & & 3 \end{pmatrix},$$

$$\hat{T}_{xa} = \frac{1}{4\sqrt{5}} \begin{pmatrix} & -\sqrt{3} & & 5 \\ -\sqrt{3} & & 3 & \\ & 3 & & -\sqrt{3} \\ 5 & & -\sqrt{3} & \end{pmatrix},$$

$$\hat{T}_{xyz} = \frac{i}{2} \begin{pmatrix} & & -1 & \\ & & & 1 \\ 1 & & & \\ & -1 & & \end{pmatrix}$$

in the $j = 3/2$ subspace and

$$\hat{J}_z = \frac{1}{\sqrt{70}} \begin{pmatrix} -5 & & & & & \\ & -3 & & & & \\ & & -1 & & & \\ & & & 1 & & \\ & & & & 3 & \\ & & & & & 5 \end{pmatrix},$$

$$\hat{T}_{xa} = \frac{1}{12} \begin{pmatrix} & -3 & & \frac{5}{\sqrt{2}} & & \\ -3 & & \frac{3}{\sqrt{10}} & & 2\sqrt{5} & \\ & \frac{3}{\sqrt{10}} & & \frac{6}{\sqrt{5}} & & \frac{5}{\sqrt{2}} \\ \frac{5}{\sqrt{2}} & & \frac{6}{\sqrt{5}} & & \frac{3}{\sqrt{10}} & \\ & 2\sqrt{5} & & \frac{3}{\sqrt{10}} & & -3 \\ & & \frac{5}{\sqrt{2}} & & -3 & \end{pmatrix},$$

$$\hat{T}_{xyz} = \frac{i}{2\sqrt{6}} \begin{pmatrix} & & -\sqrt{5} & & & \\ & & & -1 & & \\ \sqrt{5} & & & & 1 & \\ & 1 & & & & \sqrt{5} \\ & & -1 & & & \\ & & & -\sqrt{5} & & \end{pmatrix}$$

in the $j = 5/2$ subspace. All multipole matrices are normalized with $Q_{lm}^{j\Gamma\alpha} \to Q_{lm}^{j\Gamma\alpha} / \sqrt{\sum_{l'm'} |Q_{l'm'}^{j\Gamma\alpha}|^2}$. For two-dimensional IR $E_g^{\pm}$, we fix the sign in the definition of its two components so $\hat{Q}_r^{j_1\Gamma\alpha} \hat{Q}_r^{j_2\Gamma\beta} \equiv (\hat{Q}_x^{j_1\Gamma\alpha} \hat{Q}_x^{j_2\Gamma\beta} + \hat{Q}_y^{j_1\Gamma\alpha} \hat{Q}_y^{j_2\Gamma\beta})/2$ belongs to the identity representation.

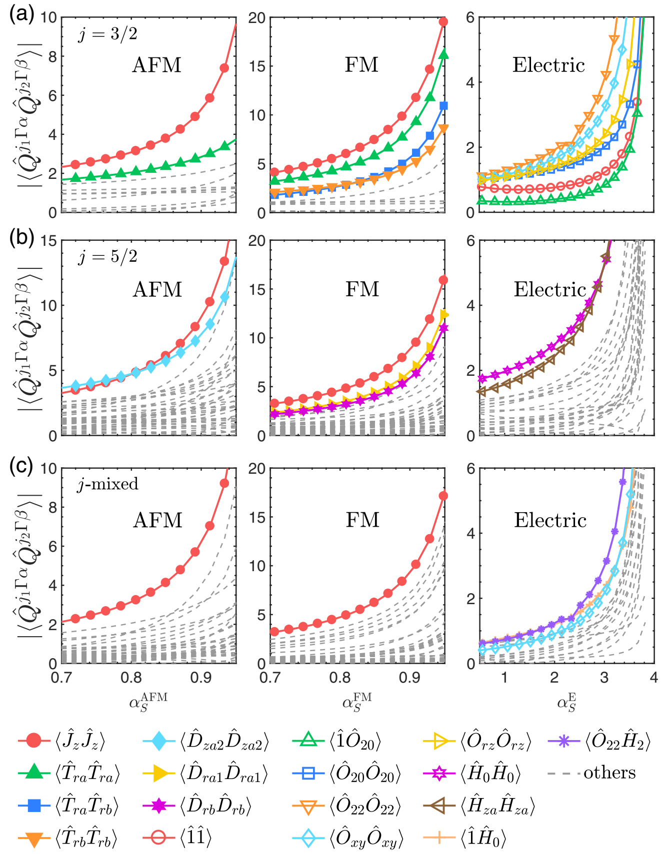

FIG. 5. (a) Evolution of 11 AFM and FM magnetic multipole correlations and six electric ones as functions of the Stoner factor α_S at their respective wave vector for $j = 3/2$. (b) Evolution of 38 AFM and FM magnetic multipole correlations and 23 electric ones as functions of their respective α_S for $j = 5/2$. (c) Evolution of 30 AFM and FM magnetic multipole correlations and 15 electric ones as functions of their respective α_S for j-mixed subspace.

APPENDIX B: LEADING RPA MULTIPOLE FLUCTUATIONS

We evaluate the dynamical susceptibility $\hat{\chi}^{\mathrm{RPA}}$ from RPA, project it into the j space, and define an effective strength for each multipole channel using the correlation function [56,99]:

$$\langle \hat{Q}^{j_1\Gamma\alpha} \hat{Q}^{j_2\Gamma\beta} \rangle = \sum_{lml'm'} Q_{ml}^{j_1\Gamma\alpha} [\hat{\chi}^{\mathrm{RPA}}]_{mm'}^{ll'}(\mathbf{Q}, \omega \to 0) Q_{l'm'}^{j_2\Gamma\beta}. \tag{B1}$$

The RPA susceptibility $\hat{\chi}^{\mathrm{RPA}}$ is given by

$$\hat{\chi}^{\mathrm{RPA}}(q) = [1 - \hat{\Gamma}_0 \hat{\chi}_0(q)]^{-1} \hat{\chi}_0(q), \tag{B2}$$

where q denotes both momentum and bosonic Matsubara frequency and $\hat{\chi}_0(q)$ is the Lindhard susceptibility:

$$[\chi_0]_{l_3 l_4}^{l_1 l_2}(q) = -T \sum_k G_{l_1 l_2}^0(k) G_{l_4 l_3}^0(k - q). \tag{B3}$$

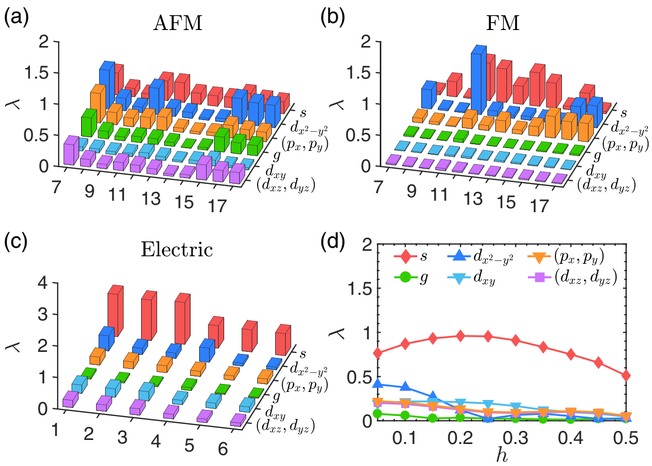

1	2	3	4	5	6	7	8	9
$\hat{\mathbb{1}}\hat{\mathbb{1}}$	$\hat{\mathbb{1}}\hat{O}_{20}$	$\hat{O}_{20}\hat{O}_{20}$	$\hat{O}_{22}\hat{O}_{22}$	$\hat{O}_{xy}\hat{O}_{xy}$	$\hat{O}_{rz}\hat{O}_{rz}$	$\hat{J}_z\hat{J}_z$	$\hat{J}_z\hat{T}_{za}$	$\hat{T}_{za}\hat{T}_{za}$
10	11	12	13	14	15	16	17	
$\hat{T}_{xyz}\hat{T}_{xyz}$	$\hat{T}_{zb}\hat{T}_{zb}$	$\hat{J}_r\hat{J}_r$	$\hat{J}_r\hat{T}_{ra}$	$\hat{J}_r\hat{T}_{rb}$	$\hat{T}_{ra}\hat{T}_{ra}$	$\hat{T}_{ra}\hat{T}_{rb}$	$\hat{T}_{rb}\hat{T}_{rb}$	

FIG. 6. Eigenvalues of six major pairing states, s (A_{1g}), $d_{x^2\text{-}y^2}$ (B_{1g}), (p_x, p_y) (E_u), g (A_{2g}), d_{xy} (B_{2g}), and (d_{xz}, d_{yz}) (E_g), for individual pairing interactions in $j = 3/2$ from (a) 11 AFM multipole fluctuation channels, (b) 11 FM channels, and (c) six electric channels. (d) Eigenvalues of six major pairing states for averaged electric multipole fluctuations as a function of $\mathbf{Q}_{\mathrm{E}}$ along $(h, h, 0)$ direction. All parameters are the same as in Fig. 2 except $\xi_z = \xi_{xy}$.

They are calculated based on the 2D TB Hamiltonian H_0 with an additional local Coulomb term,

$$H_U = \sum_i \sum_{l_1 l_2 l_3 l_4} [\Gamma_0]^{l_1 l_4}_{l_3 l_2} c^\dagger_{il_1} c^\dagger_{il_2} c_{il_3} c_{il_4}, \tag{B4}$$

where l_i represents both orbital and spin quantum numbers. The interaction matrix $\hat{\Gamma}_0$ is given by

$$\begin{aligned}
[\Gamma_0]^{ll}_{l'l'} &= [\Gamma_0]^{l'l'}_{ll} = U,\\
[\Gamma_0]^{ll'}_{ll'} &= [\Gamma_0]^{l'l}_{l'l} = -U,\\
[\Gamma_0]^{lm}_{l'm'} &= [\Gamma_0]^{l'm'}_{lm} = J,\\
[\Gamma_0]^{ll'}_{mm'} &= [\Gamma_0]^{l'l}_{m'm} = -J,\\
[\Gamma_0]^{ll}_{m'm'} &= [\Gamma_0]^{l'l'}_{mm} = U',\\
[\Gamma_0]^{lm'}_{lm'} &= [\Gamma_0]^{l'm}_{l'm} = -U',\\
[\Gamma_0]^{lm}_{m'l'} &= [\Gamma_0]^{l'm'}_{ml} = J',\\
[\Gamma_0]^{lm'}_{ml'} &= [\Gamma_0]^{l'm}_{m'l} = -J',\\
[\Gamma_0]^{ll}_{mm} &= [\Gamma_0]^{l'l'}_{m'm'} = U' - J,\\
[\Gamma_0]^{lm}_{lm} &= [\Gamma_0]^{l'm'}_{l'm'} = J - U',
\end{aligned} \tag{B5}$$

where spin up or down is distinguished by the indices with or without prime. The parameters are fixed as $J = 0.17U$, $J' = J$ and $U' = U - 2J$ according to a previous DFT+DMFT study [78]. The obtained RPA spin susceptibility peaks at $\mathbf{Q}_{\mathrm{RPA}} = (0.37, 0.37)$, close to the experimental $\mathbf{Q}_{\mathrm{AFM}}$.

Figure 5 compares the symmetry-allowed AFM, FM, and electric multipole correlations as functions of the Stoner factor α_S at their respective wave vectors. The Stoner factors are

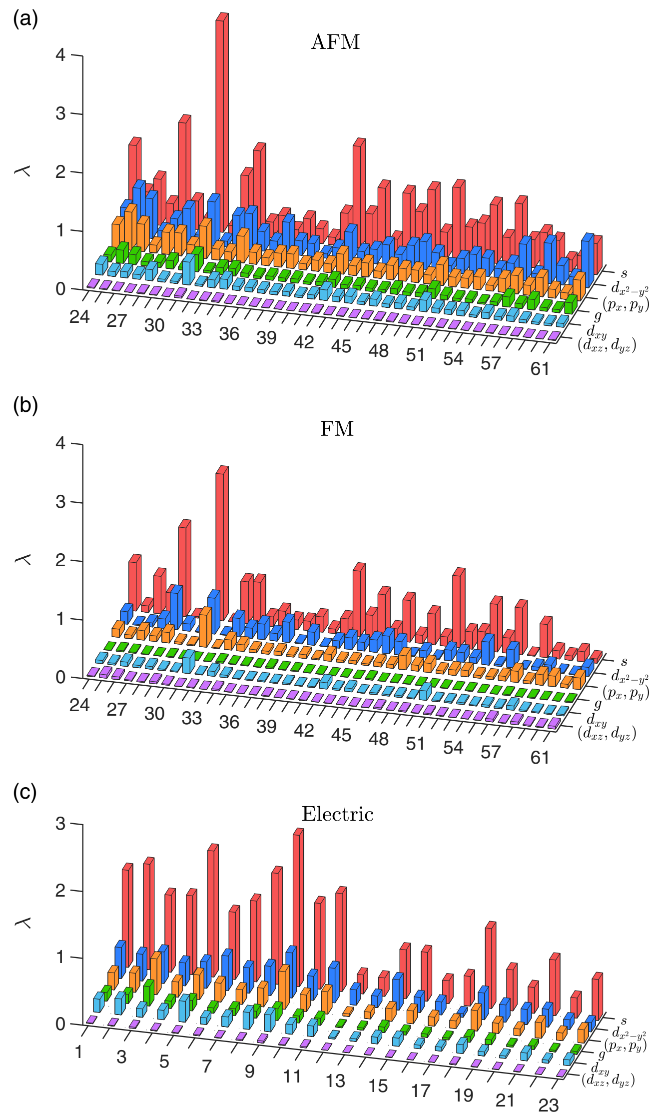

1	2	3	4	5	6	7	8	9
$\hat{\mathbb{1}}\hat{\mathbb{1}}$	$\hat{\mathbb{1}}\hat{O}_{20}$	$\hat{\mathbb{1}}\hat{H}_0$	$\hat{\mathbb{1}}\hat{H}_4$	$\hat{O}_{20}\hat{O}_{20}$	$\hat{O}_{20}\hat{H}_0$	$\hat{O}_{20}\hat{H}_4$	$\hat{H}_0\hat{H}_0$	$\hat{H}_0\hat{H}_4$
10	11	12	13	14	15	16	17	18
$\hat{H}_4\hat{H}_4$	$\hat{H}_{za}\hat{H}_{za}$	$\hat{O}_{22}\hat{O}_{22}$	$\hat{O}_{22}\hat{H}_2$	$\hat{H}_2\hat{H}_2$	$\hat{O}_{xy}\hat{O}_{xy}$	$\hat{O}_{xy}\hat{H}_{zb}$	$\hat{H}_{zb}\hat{H}_{zb}$	$\hat{O}_{rz}\hat{O}_{rz}$
19	20	21	22	23	24	25	26	27
$\hat{O}_{rz}\hat{H}_{ra}$	$\hat{O}_{rz}\hat{H}_{rb}$	$\hat{H}_{ra}\hat{H}_{ra}$	$\hat{H}_{ra}\hat{H}_{rb}$	$\hat{H}_{rb}\hat{H}_{rb}$	$\hat{D}_4\hat{D}_4$	$\hat{J}_z\hat{J}_z$	$\hat{J}_z\hat{T}_{za}$	$\hat{J}_z\hat{D}_{za1}$
28	29	30	31	32	33	34	35	36
$\hat{J}_z\hat{D}_{za2}$	$\hat{T}_{za}\hat{T}_{za}$	$\hat{T}_{za}\hat{D}_{za1}$	$\hat{T}_{za}\hat{D}_{za2}$	$\hat{D}_{za1}\hat{D}_{za1}$	$\hat{D}_{za1}\hat{D}_{za2}$	$\hat{D}_{za2}\hat{D}_{za2}$	$\hat{T}_{xyz}\hat{T}_{xyz}$	$\hat{T}_{xyz}\hat{D}_2$
37	38	39	40	41	42	43	44	45
$\hat{D}_2\hat{D}_2$	$\hat{T}_{zb}\hat{T}_{zb}$	$\hat{T}_{zb}\hat{D}_{zb}$	$\hat{D}_{zb}\hat{D}_{zb}$	$\hat{J}_r\hat{J}_r$	$\hat{J}_r\hat{T}_{ra}$	$\hat{J}_r\hat{T}_{rb}$	$\hat{J}_r\hat{D}_{ra1}$	$\hat{J}_r\hat{D}_{ra2}$
46	47	48	49	50	51	52	53	54
$\hat{J}_r\hat{D}_{rb}$	$\hat{T}_{ra}\hat{T}_{ra}$	$\hat{T}_{ra}\hat{T}_{rb}$	$\hat{T}_{ra}\hat{D}_{ra1}$	$\hat{T}_{ra}\hat{D}_{ra2}$	$\hat{T}_{ra}\hat{D}_{rb}$	$\hat{T}_{rb}\hat{T}_{rb}$	$\hat{T}_{rb}\hat{D}_{ra1}$	$\hat{T}_{rb}\hat{D}_{ra2}$
55	56	57	58	59	60	61		
$\hat{T}_{rb}\hat{D}_{rb}$	$\hat{D}_{ra1}\hat{D}_{ra1}$	$\hat{D}_{ra1}\hat{D}_{ra2}$	$\hat{D}_{ra1}\hat{D}_{rb}$	$\hat{D}_{ra2}\hat{D}_{ra2}$	$\hat{D}_{ra2}\hat{D}_{rb}$	$\hat{D}_{rb}\hat{D}_{rb}$		

FIG. 7. Comparison of six major pairing states obtained by diagonalizing the linearized Eliashberg equations on the 3D Fermi surfaces of Sr_2RuO_4 from (a) 38 AFM multipole fluctuation channels, (b) 38 FM channels, and (c) 23 electric channels for $j = 5/2$. All parameters are the same as in Fig. 2. The table on the bottom lists all multipole fluctuation channels for $j = 5/2$ sorted according to their IRs and ranks.

defined as the largest eigenvalue of the matrix $\hat{\Gamma}_0\hat{\chi}_0(q)$ for given $\mathbf{Q}$ [100]. For $j = 3/2$, we find, among all 11 magnetic multipoles, two leading components, $\langle \hat{J}_z\hat{J}_z \rangle$ and $\langle \hat{T}_{ra}\hat{T}_{ra} \rangle$, in the AFM channel, and four leading components, $\langle \hat{J}_z\hat{J}_z \rangle$, $\langle \hat{T}_{ra}\hat{T}_{ra} \rangle$,

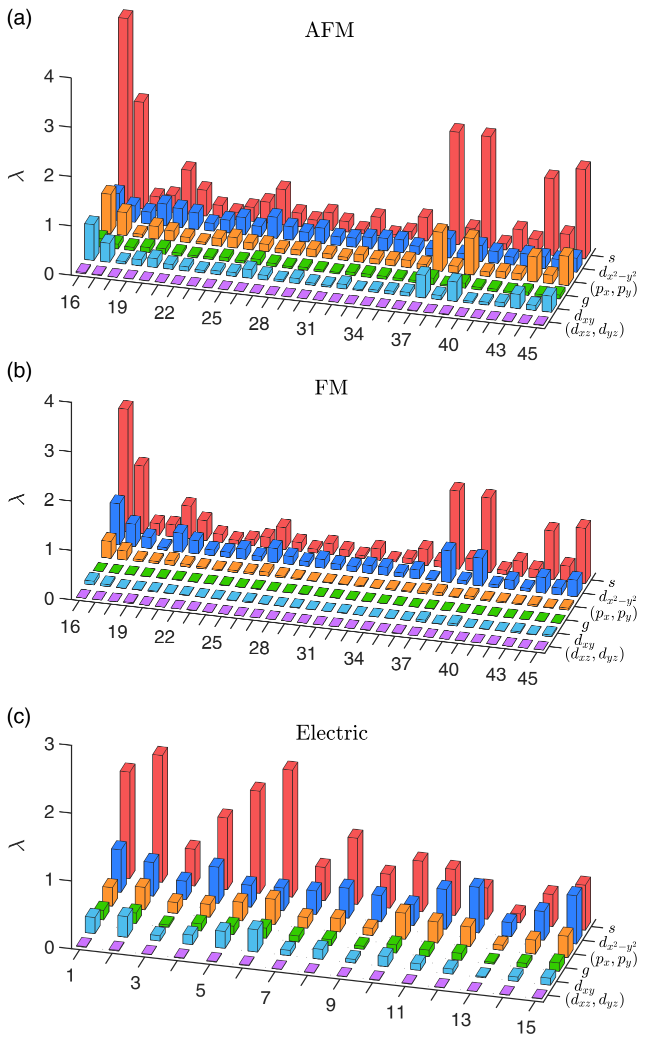

1	2	3	4	5	6	7	8	9
$\hat{\mathbb{1}}\hat{\mathbb{1}}$	$\hat{\mathbb{1}}\hat{O}_{20}$	$\hat{\mathbb{1}}\hat{H}_0$	$\hat{\mathbb{1}}\hat{H}_4$	$\hat{O}_{20}\hat{\mathbb{1}}$	$\hat{O}_{20}\hat{O}_{20}$	$\hat{O}_{20}\hat{H}_0$	$\hat{O}_{20}\hat{H}_4$	$\hat{O}_{22}\hat{O}_{22}$
10	11	12	13	14	15	16	17	18
$\hat{O}_{22}\hat{H}_2$	$\hat{O}_{xy}\hat{O}_{xy}$	$\hat{O}_{xy}\hat{H}_{zb}$	$\hat{O}_{rz}\hat{O}_{rz}$	$\hat{O}_{rz}\hat{H}_{ra}$	$\hat{O}_{rz}\hat{H}_{rb}$	$\hat{J}_z\hat{J}_z$	$\hat{J}_z\hat{T}_{za}$	$\hat{J}_z\hat{D}_{za1}$
19	20	21	22	23	24	25	26	27
$\hat{J}_z\hat{D}_{za2}$	$\hat{T}_{za}\hat{J}_z$	$\hat{T}_{za}\hat{T}_{za}$	$\hat{T}_{za}\hat{D}_{za1}$	$\hat{T}_{za}\hat{D}_{za2}$	$\hat{T}_{xyz}\hat{T}_{xyz}$	$\hat{T}_{xyz}\hat{D}_2$	$\hat{T}_{zb}\hat{T}_{zb}$	$\hat{T}_{zb}\hat{D}_{zb}$
28	29	30	31	32	33	34	35	36
$\hat{J}_r\hat{J}_r$	$\hat{J}_r\hat{T}_{ra}$	$\hat{J}_r\hat{T}_{rb}$	$\hat{J}_r\hat{D}_{ra1}$	$\hat{J}_r\hat{D}_{ra2}$	$\hat{J}_r\hat{D}_{rb}$	$\hat{T}_{ra}\hat{J}_r$	$\hat{T}_{ra}\hat{T}_{ra}$	$\hat{T}_{ra}\hat{T}_{rb}$
37	38	39	40	41	42	43	44	45
$\hat{T}_{ra}\hat{D}_{ra1}$	$\hat{T}_{ra}\hat{D}_{ra2}$	$\hat{T}_{ra}\hat{D}_{rb}$	$\hat{T}_{rb}\hat{J}_r$	$\hat{T}_{rb}\hat{T}_{ra}$	$\hat{T}_{rb}\hat{T}_{rb}$	$\hat{T}_{rb}\hat{D}_{ra1}$	$\hat{T}_{rb}\hat{D}_{ra2}$	$\hat{T}_{rb}\hat{D}_{rb}$

FIG. 8. Comparison of six major pairing states from (a) 30 AFM multipole fluctuation channels, (b) 30 FM channels, and (c) 15 electric channels in j-mixed subspace. All parameters are the same as in Fig. 2. The table on the bottom lists all multipole fluctuation channels in j-mixed subspace sorted according to their IRs and ranks.

$\langle\hat{T}_{ra}\hat{T}_{rb}\rangle$, $\langle\hat{T}_{rb}\hat{T}_{rb}\rangle$, in the FM channel. For $j = 5/2$, among all 38 magnetic multipoles, we find two leading components, $\langle\hat{J}_z\hat{J}_z\rangle$, $\langle\hat{D}_{za2}\hat{D}_{za2}\rangle$, for AFM fluctuations, and three leading components, $\langle\hat{J}_z\hat{J}_z\rangle$, $\langle\hat{D}_{ra1}\hat{D}_{ra1}\rangle$, $\langle\hat{D}_{rb}\hat{D}_{rb}\rangle$, for FM fluctuations. For j-mixed subspace, $\langle\hat{J}_z\hat{J}_z\rangle$ is the leading component for both AFM and FM fluctuations. The electric multipole fluctuations show no significant variation for $\alpha_S^{\rm E} < 1$ in all j spaces, indicating the absence of electric instability on the RPA level.

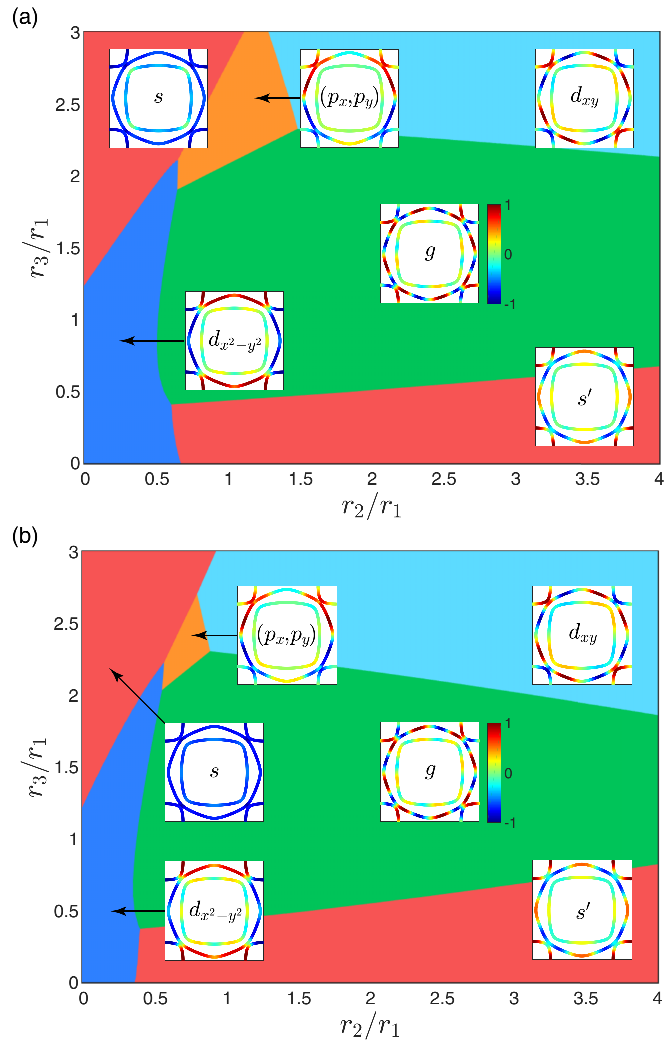

FIG. 9. Theoretical phase diagrams of the superconductivity in Sr_2RuO_4 for the mixed pairing interaction averaged over all multipole components in (a) $j = 3/2$ and (b) $j = 3/2$ and $5/2$. The insets show typical gap structures in each region. All parameters are the same as in Fig. 3.

APPENDIX C: PAIRING STATES WITH $\xi_z = \xi_{xy}$ for $j = 3/2$

Figure 6 shows six major pairing states with an artificially enlarged $\xi_z = \xi_{xy}$ for all three channels (AFM, FM, electric) in the $j = 3/2$ manifold. All other parameters are the same as in Fig. 2. A larger value of ξ_z does enhance $d_{xz} + id_{yz}$ and other m_z-antisymmetric pairing states, but it is still not enough to make them predominant. This implies the $d_{xz} + id_{yz}$ pairing is not favored for the quasi-2D superconductor Sr_2RuO_4, at least within our framework.

APPENDIX D: PAIRING STATES FOR $j = 5/2$ AND j-MIXED

Figure 7 compares the eigenvalues of six major pairing states induced by 38 AFM or FM multipole fluctuation channels and 23 electric channels for $j = 5/2$. For the FM channel, the leading dipole $\hat{J}_z\hat{J}_z$ favors the s wave, while the leading dotriacontapoles $\hat{D}_{ra1}\hat{D}_{ra1}$ and $\hat{D}_{rb}\hat{D}_{rb}$ support (p_x, p_y)

waves. Figure 8 compares the eigenvalues of six major pairing states induced by 30 AFM or FM multipole fluctuation channels and 15 electric channels for the j-mixed subspace. Most components support the s wave, including the leading component $\hat{J}_z\hat{J}_z$ for AFM and FM channels and the leading components $\hat{\mathbb{1}}\hat{H}_0$, $\hat{O}_{22}\hat{H}_2$, $\hat{O}_{xy}\hat{O}_{xy}$ for electric channels, while the rest support $d_{x^2\text{-}y^2}$. Therefore, the j-mixed components would enhance s-wave pairing in the phase diagram. We note that the off-diagonal multipole fluctuations $\hat{Q}^{j_1\Gamma\alpha}\hat{Q}^{j_2\Gamma\beta}$ with $j_1 \neq j_2$ or $\alpha \neq \beta$ may lead to negative contributions to the renormalization function Z_μ and were usually ignored in the literature [56,99–101]. They are also taken into consideration in our calculations.

APPENDIX E: ROBUSTNESS OF *g*-WAVE

Figure 9 compares the phase diagram for the pairing interactions averaged only over $j = 3/2$ and that over both $j = 3/2$ and $5/2$ without j-mixed components. The two phase diagrams are basically the same except for some slight adjustments of each pairing region, while in Fig. 3(b), all phase boundaries are pushed down toward smaller r_3/r_1 as expected once j-mixed contributions are included. Nevertheless, we still obtain a dominant g wave in the broad intermediate region and a two-component $d_{x^2-y^2} + ig$ pairing may emerge with strong AFM and moderate FM and electric multipole fluctuations.

[1] Y. Maeno, H. Hashimoto, K. Yoshida, S. Nishizaki, T. Fujita, J. G. Bednorz, and F. Lichtenberg, Superconductivity in a layered perovskite without Copper, Nature (London) **372**, 532 (1994).

[2] T. M. Rice and M. Sigrist, Sr_2RuO_4: An electronic analogue of ^{3}He? J. Phys.: Condens. Matter **7**, L643 (1995).

[3] K. Ishida, H. Mukuda, Y. Kitaoka, K. Asayama, Z. Q. Mao, Y. Mori, and Y. Maeno, Spin-triplet superconductivity in Sr_2RuO_4 identified by ^{17}O Knight shift, Nature (London) **396**, 658 (1998).

[4] A. P. Mackenzie and Y. Maeno, The superconductivity of Sr_2RuO_4 and the physics of spin-triplet pairing, Rev. Mod. Phys. **75**, 657 (2003).

[5] A. P. Mackenzie, T. Scaffidi, C. W. Hicks, and Y. Maeno, Even odder after twenty-three years: The superconducting order parameter puzzle of Sr_2RuO_4, npj Quantum Mater. **2**, 40 (2017).

[6] A. Pustogow, Y. Luo, A. Chronister, Y. S. Su, D. A. Sokolov, and F. Jerzembeck, A. P. Mackenzie, C. W. Hicks, N. Kikugawa, S. Raghu, E. D. Bauer, and S. E. Brown, Constraints on the superconducting order parameter in Sr_2RuO_4 from oxygen-17 nuclear magnetic resonance, Nature (London) **574**, 72 (2019).

[7] K. Ishida, M. Manago, K. Kinjo, and Y. Maeno, Reduction of the ^{17}O Knight Shift in the superconducting state and the heat-up effect by NMR pulses on Sr_2RuO_4, J. Phys. Soc. Jpn. **89**, 034712 (2020).

[8] A. Chronister, A. Pustogow, and N. Kikugawa, D. A. Sokolov, F. Jerzembeck, and C. W. Hicks, A. P. Mackenzie, E. D. Bauer, and S. E. Brown, Evidence for even parity unconventional superconductivity in Sr_2RuO_4, Proc. Natl. Acad. Sci. USA **118**, e2025313118 (2021).

[9] A. N. Petsch, M. Zhu, M. Enderle, Z. Q. Mao, Y. Maeno, I. I. Mazin, and S. M. Hayden, Reduction of the Spin Susceptibility in the Superconducting State of Sr_2RuO_4 Observed by Polarized Neutron Scattering, Phys. Rev. Lett. **125**, 217004 (2020).

[10] G. M. Luke, Y. Fudamoto, K. M. Kojima, M. I. Larkin, J. Merrin, B. Nachumi, Y. J. Uemura, Y. Maeno, Z. Q. Mao, Y. Mori, H. Nakamura, and M. Sigrist, Time-reversal symmetry-breaking superconductivity in Sr_2RuO_4, Nature (London) **394**, 558 (1998).

[11] J. Xia, Y. Maeno, P. T. Beyersdorf, M. M. Fejer, and A. Kapitulnik, High Resolution Polar Kerr Effect Measurements of Sr_2RuO_4: Evidence for Broken Time-Reversal Symmetry in the Superconducting State, Phys. Rev. Lett. **97**, 167002 (2006).

[12] S. NishiZaki, Y. Maeno, and Z. Mao, Changes in the superconducting state of Sr_2RuO_4 under magnetic fields probed by specific heat, J. Phys. Soc. Jpn. **69**, 572 (2000).

[13] K. Deguchi, Z. Q. Mao, H. Yaguchi, and Y. Maeno, Gap Structure of the Spin-Triplet Superconductor Sr_2RuO_4 Determined from the Field-Orientation Dependence of the Specific Heat, Phys. Rev. Lett. **92**, 047002 (2004).

[14] S. Kittaka, S. Nakamura, T. Sakakibara, N. Kikugawa, T. Terashima, S. Uji, D. A. Sokolov, A. P. Mackenzie, K. Irie, Y. Tsutsumi, K. Suzuki, and K. Machida, Searching for gap zeros in Sr_2RuO_4 via field-angle-dependent specific-heat measurement, J. Phys. Soc. Jpn. **87**, 093703 (2018).

[15] I. Bonalde, B. D. Yanoff, M. B. Salamon, D. J. Van Harlingen, E. M. E. Chia, Z. Q. Mao, and Y. Maeno, Temperature Dependence of the Penetration Depth in Sr_2RuO_4: Evidence for Nodes in the Gap Function, Phys. Rev. Lett. **85**, 4775 (2000).

[16] M. Suzuki, M. A. Tanatar, N. Kikugawa, Z. Q. Mao, Y. Maeno, and T. Ishiguro, Universal Heat Transport in Sr_2RuO_4, Phys. Rev. Lett. **88**, 227004 (2002).

[17] E. Hassinger, P. Bourgeois-Hope, H. Taniguchi, S. René de Cotret, G. Grissonnanche, M. S. Anwar, Y. Maeno, N. Doiron-Leyraud, and L. Taillefer, Vertical Line Nodes in the Superconducting Gap Structure of Sr_2RuO_4, Phys. Rev. X **7**, 011032 (2017).

[18] K. Ishida, H. Mukuda, Y. Kitaoka, Z. Q. Mao, Y. Mori, and Y. Maeno, Anisotropic Superconducting Gap in the Spin-Triplet Superconductor Sr_2RuO_4: Evidence from a Ru-NQR Study, Phys. Rev. Lett. **84**, 5387 (2000).

[19] R. Sharma, S. D. Edkins, Z. Wang, A. Kostin, C. Sow, Y. Maeno, A. P. Mackenzie, J. C. S. Davis, and V. Madhavan, Momentum-resolved superconducting energy gaps of Sr_2RuO_4 from quasiparticle interference imaging, Proc. Natl. Acad. Sci. USA **117**, 5222 (2020).

[20] S. A. Kivelson, A. C. Yuan, B. Ramshaw, and R. Thomale, A proposal for reconciling diverse experiments on the superconducting state in Sr_2RuO_4, npj Quantum Mater. **5**, 43 (2020).

[21] J. Clepkens, A. W. Lindquist, X. Liu, and H.-Y. Kee, Higher angular momentum pairings in interorbital shadowed-triplet superconductors: Application to Sr_2RuO_4, Phys. Rev. B **104**, 104512 (2021).

[22] A. T. Rømer, D. D. Scherer, I. M. Eremin, P. J. Hirschfeld, and B. M. Andersen, Knight Shift and Leading Superconducting Instability from Spin Fluctuations in Sr_2RuO_4, Phys. Rev. Lett. **123**, 247001 (2019).

[23] A. T. Rømer, A. Kreisel, M. A. Müller, P. J. Hirschfeld, I. M. Eremin, and B. M. Andersen, Theory of strain-induced magnetic order and splitting of T_c and $T_{\rm TRSB}$ in Sr_2RuO_4, Phys. Rev. B **102**, 054506 (2020).

[24] A. T. Rømer, P. J. Hirschfeld, and B. M. Andersen, Superconducting state of Sr_2RuO_4 in the presence of longer-range Coulomb interactions, Phys. Rev. B **104**, 064507 (2021).

[25] S. Bhattacharyya, A. Kreisel, X. Kong, T. Berlijn, A. T. Rømer, B. M. Andersen, and P. J. Hirschfeld, Superconducting gap symmetry from Bogoliubov quasiparticle interference analysis on Sr_2RuO_4, arXiv:2109.10712.

[26] Z. Wang, X. Wang, and C. Kallin, Spin-orbit coupling and spin-triplet pairing symmetry in Sr_2RuO_4, Phys. Rev. B **101**, 064507 (2020).

[27] T. Scaffidi, J. C. Romers, and S. H. Simon, Pairing symmetry and dominant band in Sr_2RuO_4, Phys. Rev. B **89**, 220510(R) (2014).

[28] H. S. Røising, T. Scaffidi, F. Flicker, G. F. Lange, and S. H. Simon, Superconducting order of $Sr_2RuO_4$from a three-dimensional microscopic model, Phys. Rev. Research **1**, 033108 (2019).

[29] W.-S. Wang, C.-C. Zhang, F.-C. Zhang, and Q.-H. Wang, Theory of Chiral *p*-Wave Superconductivity with Near Nodes for Sr_2RuO_4, Phys. Rev. Lett. **122**, 027002 (2019).

[30] A. Ramires and M. Sigrist, Superconducting order parameter of Sr_2RuO_4: A microscopic perspective, Phys. Rev. B **100**, 104501 (2019).

[31] T. Scaffidi, Degeneracy between even- and odd-parity superconductivity in the quasi-1D Hubbard model and implications for Sr_2RuO_4, arXiv:2007.13769,

[32] R. Gupta, T. Saunderson, S. Shallcross, M. Gradhand, J. Quintanilla, and J. Annett, Superconducting subphase and substantial Knight shift in Sr_2RuO_4, Phys. Rev. B **102**, 235203 (2020).

[33] S. Ikegaya, K. Yada, Y. Tanaka, S. Kashiwaya, Y. Asano, and D. Manske, Identification of spin-triplet superconductivity through a helical-chiral phase transition in Sr_2RuO_4 thin films, Phys. Rev. B **101**, 220501(R) (2020).

[34] W. Chen and J. An, Interorbital *p*- and *d*-wave pairings between $d_{xz/yz}$ and d_{xy} orbitals in Sr_2RuO_4, Phys. Rev. B **102**, 094501 (2020).

[35] W. Huang and Z. Wang, Possibility of mixed helical p-wave pairings in Sr_2RuO_4, Phys. Rev. Research **3**, L042002 (2021).

[36] S.-J. Zhang, D. Wang, and Q.-H. Wang, Possible two-component spin-singlet pairings in Sr_2RuO_4, Phys. Rev. B **104**, 094504 (2021).

[37] O. Gingras, R. Nourafkan, A.-M. S. Tremblay, and M. Côté, Superconducting Symmetries of Sr_2RuO_4 from First-Principles Electronic Structure, Phys. Rev. Lett. **123**, 217005 (2019).

[38] H. G. Suh, H. Menke, P. M. R. Brydon, C. Timm, A. Ramires, and D. F. Agterberg, Stabilizing even-parity chiral superconductivity in Sr_2RuO_4, Phys. Rev. Research **2**, 032023(R) (2020).

[39] W. Huang, Y. Zhou, and H. Yao, Exotic Cooper pairing in multiorbital models of Sr_2RuO_4, Phys. Rev. B **100**, 134506 (2019).

[40] S.-O. Kaba and D. Sénéchal, Group-theoretical classification of superconducting states of strontium ruthenate, Phys. Rev. B **100**, 214507 (2019).

[41] S. Käser, H. U. R. Strand, N. Wentzell, A. Georges, O. Parcollet, and P. Hansman, Inter-orbital singlet pairing in Sr_2RuO_4: A Hund's superconductor, Phys. Rev. B **105**, 155101 (2022).

[42] J.-L. Zhang, Y. Li, W. Huang, and F.-C. Zhang, Hidden anomalous Hall effect in Sr_2RuO_4 with chiral superconductivity dominated by the Ru d_{xy} orbital, Phys. Rev. B **102**, 180509(R) (2020).

[43] S. Ghosh, A. Shekhter, F. Jerzembeck, N. Kikugawa, D. A. Sokolov, M. Brando, A. P. Mackenzie, C. W. Hicks, and B. J. Ramshaw, Thermodynamic evidence for a two-component superconducting order parameter in Sr_2RuO_4, Nat. Phys. **17**, 199 (2021).

[44] S. Benhabib, C. Lupien, I. Paul, L. Berges, M. Dion, M. Nardone, A. Zitouni, Z. Q. Mao, Y. Maeno, A. Georges, L. Taillefer, and C. Proust, Ultrasound evidence for a two-component superconducting order parameter in Sr_2RuO_4, Nat. Phys. **17**, 194 (2021).

[45] V. Grinenko, S. Ghosh, R. Sarkar, J.-C. Orain, A. Nikitin, M. Elender, D. Das, Z. Guguchia, F. Brückner, M. E. Barber, J. Park, N. Kikugawa, D. A. Sokolov, J. S. Bobowski, T. Miyoshi, Y. Maeno, A. P. Mackenzie, H. Luetkens, C. W. Hicks, and H.-H. Klauss, Split superconducting and time-reversal symmetry-breaking transitions in Sr_2RuO_4 under stress, Nat. Phys. **17**, 748 (2021).

[46] V. Grinenko, D. Das, R. Gupta, B. Zinkl, N. Kikugawa, Y. Maeno, C. W. Hicks, H.-H. Klauss, M. Sigrist, and R. Khasanov, Unsplit superconducting and time reversal symmetry breaking transitions in Sr_2RuO_4 under hydrostatic pressure and disorder, Nat. Commun. **12**, 3920 (2021).

[47] Y.-S. Li, N. Kikugawa, D. A. Sokolov, F. Jerzembeck, A. S. Gibbs, Y. Maeno, C. W. Hicks, J. Schmalian, M. Nicklas, and A. P. Mackenzie, High-sensitivity heat-capacity measurements on Sr_2RuO_4 under uniaxial pressure, Proc. Natl. Acad. Sci. USA **118**, e2020492118 (2021).

[48] A. C. Yuan, E. Berg, and S. A. Kivelson, Strain-induced time reversal breaking and half quantum vortices near a putative superconducting tetracritical point in Sr_2RuO_4, Phys. Rev. B **104**, 054518 (2021).

[49] R. Willa, M. Hecker, R. M. Fernandes, J. Schmalian, Inhomogeneous time-reversal symmetry breaking in Sr_2RuO_4, Phys. Rev. B **104**, 024511 (2021).

[50] C. N. Veenstra, Z.-H. Zhu, M. Raichle, B. M. Ludbrook, A. Nicolaou, B. Slomski, G. Landolt, S. Kittaka, Y. Maeno, J. H. Dil, I. S. Elfimov, M. W. Haverkort, and A. Damascelli, Spin-Orbital Entanglement and the Breakdown of Singlets and Triplets in Sr_2RuO_4 Revealed by Spin- and Angle-Resolved Photoemission Spectroscopy, Phys. Rev. Lett. **112**, 127002 (2014).

[51] G. Zhang, E. Gorelov, E. Sarvestani, and E. Pavarini, Fermi Surface of Sr_2RuO_4: Spin-Orbit and Anisotropic Coulomb Interaction Effects, Phys. Rev. Lett. **116**, 106402 (2016).

[52] K. W. H. Stevens, Matrix elements and operator equivalents connected with the magnetic properties of rare earth ions, Proc. Phys. Soc. A **65**, 209 (1952).
[53] T. Inui, Y. Tanabe, and Y. Onodera, *Group Theory and Its Applications in Physics* (Springer, Berlin, 1990).
[54] H. Kusunose, Description of multipole in f-electron systems, J. Phys. Soc. Jpn. **77**, 064710 (2008).
[55] H. Watanabe and Y. Yanase, Group-theoretical classification of multipole order: Emergent responses and candidate materials, Phys. Rev. B **98**, 245129 (2018).
[56] H. Ikeda, M.-T. Suzuki, R. Arita, T. Takimoto, T. Shibauchi, and Y. Matsuda, Emergent rank-5 nematic order in URu_2Si_2, Nat. Phys. **8**, 528 (2012).
[57] F. C. von der Lage, and H. A. Bethe, A method for obtaining electronic eigenfunctions and eigenvalues in solids with an application to sodium, Phys. Rev. **71**, 612 (1947).
[58] G. Khaliullin, Excitonic Magnetism in Van Vleck-Type d^4 Mott Insulators, Phys. Rev. Lett. **111**, 197201 (2013).
[59] L. Das, F. Forte, R. Fittipaldi, C. G. Fatuzzo, V. Granata, O. Ivashko, M. Horio, F. Schindler, M. Dantz, Yi Tseng, D. E. McNally, H. M. Rønnow, W. Wan, N. B. Christensen, 6 J. Pelliciari, P. Olalde-Velasco, N. Kikugawa, T. Neupert, A. Vecchione, T. Schmitt *et al.*, Spin-Orbital Excitations in Ca_2RuO_4 Revealed by Resonant Inelastic x-Ray Scattering, Phys. Rev. X **8**, 011048 (2018).
[60] V. Zabolotnyy, D. Evtushinsky, A. Kordyuk, T. Kim, E. Carleschi, B. Doyle, R. Fittipaldi, M. Cuoco, A. Vecchione, and S. Borisenko, Renormalized band structure of Sr_2RuO_4: A quasiparticle tight-binding approach, J. Electron Spectrosc. Relat. Phenom. **191**, 48 (2013).
[61] E. Pavarini and I. I. Mazin, First-principles study of spin-orbit effects and NMR in Sr_2RuO_4, Phys. Rev. B **74**, 035115 (2006).
[62] Y. Sidis, M. Braden, P. Bourges, B. Hennion, S. NishiZaki, Y. Maeno, and Y. Mori, Evidence for Incommensurate Spin Fluctuations in Sr_2RuO_4, Phys. Rev. Lett. **83**, 3320 (1999).
[63] F. Servant, S. Raymond, B. Fåk, P. Lejay, and J. Flouquet, Two-dimensional spin fluctuations in Sr_2RuO_4, Solid State Commun. **116**, 489 (2000).
[64] P. Steffens, Y. Sidis, J. Kulda, Z. Q. Mao, Y. Maeno, I. I. Mazin, and M. Braden, Spin Fluctuations in Sr_2RuO_4 from Polarized Neutron Scattering: Implications for Superconductivity, Phys. Rev. Lett. **122**, 047004 (2019).
[65] A. J. Millis, H. Monien, and D. Pines, Phenomenological model of nuclear relaxation in the normal state of $YBa_2Cu_3O_7$, Phys. Rev. B **42**, 167 (1990).
[66] P. Monthoux, A. V. Balatsky, and D. Pines, Toward a Theory of High-Temperature Superconductivity in the Antiferromagnetically Correlated Cuprate Oxides, Phys. Rev. Lett. **67**, 3448 (1991).
[67] P. Monthoux and D. Pines, Spin-Fluctuation-Induced Superconductivity in the Copper Oxides: A Strong Coupling Calculation, Phys. Rev. Lett. **69**, 961 (1992).
[68] C. M. Varma, Considerations on the mechanisms and transition temperatures of superconductivity induced by electronic fluctuations, Rep. Prog. Phys. **75**, 052501 (2012).
[69] Y.-F. Yang and D. Pines, Emergence of superconductivity in heavy-electron materials, Proc. Natl. Acad. Sci. USA **111**, 18178 (2014).
[70] Y. Li and Y.-F. Yang, A phenomenological theory of heavy fermion superconductivity in $CeCoIn_5$, Chin. Sci. Bull. **62**, 4068 (2017).
[71] Y. Li, M. Liu, Z. Fu, X. Chen, F. Yang, and Y.-F. Yang, Gap Symmetry of the Heavy Fermion Superconductor $CeCu_2Si_2$ at Ambient Pressure, Phys. Rev. Lett. **120**, 217001 (2018).
[72] Y. Li, Q. Wang, Y. Xu, W. Xie, and Y.-F. Yang, Nearly degenerate $p_x + ip_y$ and $d_{x^2-y^2}$ pairing symmetry in the heavy fermion superconductor $YbRh_2Si_2$, Phys. Rev. B **100**, 085132 (2019).
[73] Z. Liu, Y. Li, and Y.-F. Yang, Possible nodeless $s^{\pm}$-wave superconductivity in twisted bilayer graphene, Chin. Phys. B **28**, 077103 (2019).
[74] Y. Li, Y.-T. Sheng, and Y.-F. Yang, Theoretical progress and material studies of heavy fermion superconductors, Acta Phys. Sin. **70**, 017402 (2021).
[75] C. Bergemann, A. P. Mackenzie, S. R. Julian, D. Forsythe, and E. Ohmichi, Quasi-two-dimensional Fermi liquid properties of the unconventional superconductor Sr_2RuO_4, Adv. Phys. **52**, 639 (2003).
[76] J. E. Ortmann, J. Y. Liu, J. Hu, M. Zhu, J. Peng, M. Matsuda, X. Ke, and Z. Q. Mao, Competition between antiferromagnetism and ferromagnetism in Ca_2RuO_4 probed by Mn and Co doping, Sci. Rep. **3**, 2950 (2013).
[77] S. Raghu, A. Kapitulnik, and S. A. Kivelson, Hidden Quasi-One-Dimensional Superconductivity in Sr_2RuO_4, Phys. Rev. Lett. **105**, 136401 (2010).
[78] J. Mravlje, M. Aichhorn, T. Miyake, K. Haule, G. Kotliar, and A. Georges, Coherence-Incoherence Crossover and the Mass-Renormalization Puzzles in Sr_2RuO_4, Phys. Rev. Lett. **106**, 096401 (2011).
[79] S. Acharya, M. S. Laad, D. Dey, T. Maitra, and A. Taraphder, First-principles correlated approach to the normal state of strontium ruthenate, Sci. Rep. **7**, 43033 (2017).
[80] L. Boehnke, P. Werner, and F. Lechermann, Multi-orbital nature of the spin fluctuations in Sr_2RuO_4, Europhys. Lett. **122**, 57001 (2018).
[81] S. Acharya, D. Pashov, C. Weber, H. Park, L. Sponza, and M. V. Schilfgaarde, Evening out the spin and charge parity to increase T_c in Sr_2RuO_4, Commun. Phys. **2**, 163 (2019).
[82] Y. Feng, J. Wang, R. Jaramillo, J. van Wezel, S. Haravifard, G. Srajer, Y. Liu, Z.-A. Xu, P. B. Littlewood, and T. F. Rosenbaum, Order parameter fluctuations at a buried quantum critical point, Proc. Natl. Acad. Sci. USA **109**, 7224 (2012).
[83] T. P. Croft, C. Lester, M. S. Senn, A. Bombardi, and S. M. Hayden, Charge density wave fluctuations in $La_{2-x}Sr_xCuO_4$ and their competition with superconductivity, Phys. Rev. B **89**, 224513 (2014).
[84] Y. Gallais, R. M. Fernandes, I. Paul, L. Chauvière, Y.-X. Yang, M.-A. Méasson, M. Cazayous, A. Sacuto, D. Colson, and A. Forget, Observation of in $Ba(Fe_{1-x}Co_x)_2As_2$, Phys. Rev. Lett. **111**, 267001 (2013).
[85] X. Xi, L. Zhao, Z. Wang, H. Berger, L. Forró, J. Shan, and K. F. Mak, Strongly enhanced charge-density-wave order in monolayer $NbSe_2$, Nat. Nanotechnol. **10**, 765 (2015).
[86] V. K. Thorsmølle, M. Khodas, Z. P. Yin, C. Zhang, S. V. Carr, P. Dai, and G. Blumberg, Critical quadrupole fluctuations and collective modes in iron pnictide superconductors, Phys. Rev. B **93**, 054515 (2016).

[87] Y. Yu, A. K. C. Cheung, S. Raghu, and D. F. Agterberg, Residual spin susceptibility in the spin-triplet orbital-singlet model, Phys. Rev. B **98**, 184507 (2018).
[88] A. W. Lindquist and H.-Y. Kee, Distinct reduction of Knight shift in superconducting state of Sr_2RuO_4 under uniaxial strain, Phys. Rev. Research **2**, 032055(R) (2020).
[89] Y. Fukaya, T. Hashimoto, M. Sato, Y. Tanaka, and K. Yada, Spin susceptibility for orbital-singlet Cooper pair in the three-dimensional Sr_2RuO_4 superconductor, Phys. Rev. Research **4**, 013135 (2022).
[90] A. Ramires, Nodal gaps from local interactions in Sr_2RuO_4, J. Phys. Conf. Ser. **2164**, 012002 (2022).
[91] K. Iida, M. Kofu, K. Suzuki, N. Murai, S. Ohira-Kawamura, R. Kajimoto, Y. Inamura, M. Ishikado, S. Hasegawa, T. Masuda, Y. Yoshida, K. Kakurai, K. Machida, and S. Lee, Horizontal line nodes in Sr_2RuO_4 proved by spin resonance, J. Phys. Soc. Jpn. **89**, 053702 (2020).
[92] K. Jenni, S. Kunkemöller, P. Steffens, Y. Sidis, R. Bewley, Z. Q. Mao, Y. Maeno, and M. Braden, Neutron scattering studies on spin fluctuations in Sr_2RuO_4, Phys. Rev. B **103**, 104511 (2021).
[93] Y. Hashitani, K. K. Tanaka, H. Adachi, and M. Ichioka, Variation of zero-energy density of states of a d-wave superconductor in a rotating in-plane magnetic field: Effect of nonmagnetic impurities, Phys. Rev. B **101**, 060501(R) (2020).
[94] B. Zinkl and M. Sigrist, Impurity-induced double transitions for accidentally degenerate unconventional pairing states, Phys. Rev. Research **3**, L012004 (2021).
[95] G. Wagner, H. S. Røising, F. Flicker, and S. H. Simon, Microscopic Ginzburg-Landau theory and singlet ordering in Sr_2RuO_4, Phys. Rev. B **104**, 134506 (2021).
[96] R. Shiina, H. Shiba, and P. Thalmeier, Magnetic-field effects on quadrupolar ordering in a Γ_8-quartet System CeB_6, J. Phys. Soc. Jpn. **66**, 1741 (1997).
[97] Y. Kuramoto, H. Kusunose, and A. Kiss, Multipole orders and fluctuations in strongly correlated electron systems, J. Phys. Soc. Jpn. **78**, 072001 (2009).
[98] R. Shiina, Multipolar moments in Pr-based filled-skutterudite Compounds with singlet-triplet crystal-field levels, J. Phys. Soc. Jpn. **73**, 2257 (2004).
[99] T. Nomoto and H. Ikeda, Fermi surface evolution and d-wave superconductivity in $CeCoIn_5$: Analysis based on LDA+DMFT method, Phys. Rev. B **90**, 125147 (2014).
[100] R. Tazai and H. Kontani, Fully gapped s-wave superconductivity enhanced by magnetic criticality in heavy-fermion systems, Phys. Rev. B **98**, 205107 (2018).
[101] R. Tazai and H. Kontani, Hexadecapole fluctuation mechanism for s-wave heavy fermion superconductor $CeCu_2Si_2$: Interplay between intra- and inter-orbital cooper pairs, J. Phys. Soc. Jpn. **88**, 063701 (2019).